



HAL
open science

An energy model for the transient flow boiling crisis under highly subcooled conditions at atmospheric pressure

R. Nop, Marie-Christine Duluc, N. Dorville, A. Kossolapov, F. Chavagnat, M. Bucci

► To cite this version:

R. Nop, Marie-Christine Duluc, N. Dorville, A. Kossolapov, F. Chavagnat, et al.. An energy model for the transient flow boiling crisis under highly subcooled conditions at atmospheric pressure. International Journal of Thermal Sciences, 2021, 168, pp.107042. 10.1016/j.ijthermalsci.2021.107042 . hal-03605923

HAL Id: hal-03605923

<https://cnam.hal.science/hal-03605923>

Submitted on 24 May 2023

HAL is a multi-disciplinary open access archive for the deposit and dissemination of scientific research documents, whether they are published or not. The documents may come from teaching and research institutions in France or abroad, or from public or private research centers.

L'archive ouverte pluridisciplinaire **HAL**, est destinée au dépôt et à la diffusion de documents scientifiques de niveau recherche, publiés ou non, émanant des établissements d'enseignement et de recherche français ou étrangers, des laboratoires publics ou privés.



Distributed under a Creative Commons Attribution - NonCommercial 4.0 International License

An energy model for the transient flow boiling crisis under highly subcooled conditions at atmospheric pressure

Nop R.^{a, b, c}, Duluc M.-C.^{b, d}, Dorville N.^a, Kossolapov A.^c, Chavagnat F.^c, and Bucci M.^c

^aUniversité Paris-Saclay, CEA, Service de thermo-hydraulique et de mécanique des fluides, 91191, Gif-sur-Yvette, France.

^bUniversité Paris-Saclay, CNRS, Laboratoire Interdisciplinaire des Sciences du Numériques, 91400, Orsay, France.

^cDepartment of Nuclear Science and Engineering, Massachusetts Institute of Technology, Cambridge MA 02139, USA

^dConservatoire National des Arts et Métiers, 75003, Paris, France

Abstract

We present an original model describing the transient flow boiling crisis of water at high subcooling and atmospheric pressure. We hypothesize that in such conditions, the mechanism of the boiling crisis is the prevention of the bubbles recondensation when a thin fluid layer near the heated wall reaches temperature saturation conditions. To capture this phenomenon, we propose an energy model describing the heat exchanges in the thin fluid layer throughout the entire transient from the initiation to the boiling crisis. We bring to light a non-dimensional mathematical relation capturing 168 working points in the investigated range of power escalation period (from 5 to 500 ms), subcooling (from 25 to 75 K) and Reynolds number (8,500 to 35,000) at atmospheric pressure. Its fitting accuracy is excellent for the high subcooling (50 K and above): more than 75 % of these points are predicted with ± 5 % error. This relationship enables the prediction of the transient critical heat flux based on the steady-state value or a single tuning constant. The non-dimensional groups deduced from the study are relevant tools to identify the major physical phenomena involved in transient boiling crisis and to quantify the impact of the different operating parameters.

Keywords: Subcooled flow boiling crisis, Critical Heat Flux, Exponential power escalation, Critical energy model

26 Nomenclature

27 Roman letters

28	c_p	Specific heat	$[J.kg^{-1}.K^{-1}]$
29	e	Channel half width	$[m]$
30	E'''	Energy density rise	$[J.m^{-3}]$
31	E_0'''	Bulk energy density	$[J.m^{-3}]$
32	E_{cr}'''	Critical energy density rise	$[J.m^{-3}]$
33	L	Heated length	$[m]$
34	N_x	Streamwise characteristic number of the mantle	$[-]$
35	N_y	Transverse characteristic number of the mantle	$[-]$
36	P	Probability density function of turbulent velocity fluctuations	$[-]$
37	p	Pressure	$[bar]$
38	Pr	Prandtl number	$[-]$
39	q_w''	Heat flux to water	$[W.m^{-2}]$
40	Re	Reynolds number	$[-]$
41	Re_τ	Wall Reynolds number	$[-]$
42	u^*	Wall shear velocity	$[m.s^{-1}]$
43	u_m	Mean velocity in the streamwise direction within the mantle (Eq. 12)	$[m.s^{-1}]$
44	v_m	Characteristic transverse velocity in the mantle (Eq. 19)	$[m.s^{-1}]$

45 Greek letters

46	α	Thermal diffusivity	$[m^2.s^{-1}]$
47	ΔT_{sub}	Subcooling	$[K]$
48	δ	Mantle thickness	$[m]$

49	$\delta_\nu = \nu/u^*$	Viscous sublayer unit	[m]
50	$\delta_T = \delta_\nu/Pr$	Thermal sublayer unit	[m]
51	λ	Heat removal ratio at steady-state (Eq. 23)	[-]
52	ν	Kinematic viscosity	[m ² .s ⁻¹]
53	ρ_l	Liquid density	[kg.m ⁻³]
54	τ	Period of the exponential power excursion	[s]
55	$\tau_x = L/u_{m,\infty}$	Time scale of the streamwise advection	[s]
56	Superscript		
57	*	Normalized variables relevant to the model (Eq. 10)	
58	+	Quantity normalized with the viscous sublayer Unit	
59	++	Quantity normalized with the thermal sublayer unit	
60	Subscript		
61	∞	Steady-state (related to δ when τ tending to infinity)	
62	SS	Steady-state	
63	Acronym		
64	CHF	Critical Heat Flux	
65	DNS	Direct Numerical Simulation	
66	FDNB	Fully Developed Nucleate Boiling	
67	HSIR	High Speed InfraRed Camera	
68	HSV	High Speed Visible Camera	
69	ITO	Indium Tin Oxide	
70	LSD	Liquid Sublayer Dryout	
71	NCC	Nucleation-Condensation Cycle	

72	ONB	Onset of Nucleate Boiling
73	OV	Overshoot
74	PDF	Probability Density Function
75	PWR	Pressurized Water Reactor

76 **1 Introduction**

77 In case of a fast insertion of reactivity in the core of a nuclear reactor important enough to reach
78 a prompt-critical state, *e.g.* due to a rapid ejection of the control rods, the reactor power can in-
79 crease drastically. The heat generation inside the nuclear rods may increase exponentially in time as
80 $q''' \propto e^{t/\tau}$, with the power escalation period τ resulting from the reactivity inserted and the neutronic
81 characteristics of the reactor. This time scale ranges from a few to a few hundreds milliseconds. The
82 power escalation can be mitigated by different neutronic feedback effects. In reactors with low-
83 enriched fuel such as Pressurized Water Reactors (PWRs), the Doppler effect is typically sufficient
84 to mitigate the power escalation before reaching a temperature level sufficient to cause fuel damage.
85 Conversely, in most pool-type research reactors, the fuel is highly enriched (20 % and higher) and
86 the Doppler effect may not have a sufficiently strong impact. The dominant neutronic feedback is
87 instead the so-called moderator effect due to the water density, which is largely emphasized when
88 vapor phase, *i.e.* void, is produced. The reader interested in the relevant neutronic feedback in such
89 scenario may refer to the book of Wu [1]. In most pool-type reactors, low pressure (a few bars)
90 and high subcooling (50 K or higher) facilitate the production of void during nucleate boiling. This
91 regime is the most desirable one for nuclear safety during these transients as it allows a high heat
92 removal combined with strong vapor production, which introduces a favorable reactivity feedback.
93 However, a too severe power escalation may lead to the boiling crisis and the transition to film
94 boiling would have two consequences. The void production, *i.e.* vapor, is drastically reduced and
95 so the power mitigation. The heat removal is also deteriorated triggering a significant temperature
96 rise of the fuel rod which could possibly lead to its failure. This accidental scenario is the so-called
97 BORAX-type accident. For this reason, an accurate prediction and a better physical understanding
98 of the boiling crisis under pool-type reactor conditions and under an exponential power excursion is
99 a key issue for nuclear safety.

101 Several full size reactors have been developed in the past to investigate thermohydraulic phenom-
102 ena induced by exponentially heating conditions: BORAX [2] , SPERT-I [3] and SPERT-IV [4] in the
103 USA, NSRR [5] in Japan and CABRI [6] in France. These experiments provide a realistic overview
104 of the system behavior during such accidental scenarii, as they are real nuclear cores which combine
105 thermal hydraulics and neutronics coupling. However, these integral experiments are extremely ex-
106 pensive to design and build and local information on temperature or heat flux fields is inherently
107 unavailable, nor photographic access to observe bubble dynamics. The need to gather this kind of
108 information has led to the development of small-size experiments. Only a few works investigated
109 flow boiling crisis of water at atmospheric pressure under exponential power escalation, *e.g.* Johnson
110 [7], Kataoka et al. [8] and Kossolapov et al. [9]. Johnson used resistance-based diagnostic giving
111 a mean temperature and heat flux at the wall and X-ray radiography to estimate the void fraction
112 near the heating wall. Kataoka et al. also used resistance-based diagnostic for thermal information.
113 Recently, Kossolapov et al. provided a fine observation of the process leading to boiling crisis in such
114 conditions using high-speed video and infrared thermometry with high spatial resolution.

115

116 Most of the modeling efforts regarding the flow boiling crisis focused on steady-state conditions.
117 Many reviews on the subject have been published *e.g.* by Celata [10, 11], Kandlikar [12], Zhang and
118 Mudawar [13] or Ahmed [14]. In the last decades, one of the most featured approach is the so-called
119 *Liquid Sublayer Dryout* (LSD) assuming that bubbles generated at the wall depart and form vapor
120 blankets which are then advected by the flow. The latter are located in a superheated fluid layer and
121 separated from the heating wall by a liquid layer called liquid sublayer, or macrolayer. The boiling
122 crisis is assumed to occur when the heat flux at the wall is high enough to vaporize the entire liquid
123 sublayer during the transit of a vapor blanket. Inspired by the original work of Haramura and Katto
124 [15] who investigated the saturated pool and flow boiling conditions, Lee & Mudawar [16] and then
125 Katto [17] extended this idea to subcooled flow boiling. Celata [18], starting from a similar model,
126 used thorough physical considerations to improve this approach and circumvent the experimental
127 tuning constants.

128 However, CHF models dedicated to transient heating conditions are scarce. To extend the applicabil-
129 ity of steady-state LSD models, Serizawa [19] proposed to explain the generally observed enhancement
130 between the transient and the steady-state CHF by the time needed to vaporize the liquid sublayer.
131 The problem is then reduced to the determination of this time scale. This model makes use of several
132 constants which must be determined through experiments. A few years later, Pasamehmetoglu [20]

133 improved the model, in particular by including turbulence effects of the flow. Besides, due to the
134 limitations of instrumentation at that time, experimental data used by Serizawa and Pasamehme-
135 toglu to develop their models were intrinsically space-averaged values. For fast transients, these
136 averaged values only provide limited information. The Liquid Sublayer Dryout phenomenology was
137 then generalized for conditions for which no experimental observation of the mechanism involved in
138 the boiling crisis could be done, *e.g.* bubbles do not necessarily depart.

139

140 The work of Kossolapov et al. [9] gives a new insight on the underlying mechanisms. It reveals
141 in particular that, for high subcoolings, neither departure of the bubbles from the wall to the core
142 of the flow, nor the formation of vapor blankets are observed. Therefore, the LSD approach used
143 by Serizawa [19] and Pasamehmetoglu [20] as described above is not applicable for highly subcooled
144 conditions which are yet relevant for pool-type research reactors. In summary, there seem to be no
145 models applicable to BORAX-type accidents in highly subcooled water. Filling this gap is of key
146 importance for nuclear safety.

147

148 Based on our understanding of the data gathered by Kossolapov et al., we propose a new model
149 for the description of the transient boiling crisis, suitable for forced convection, highly subcooled flow
150 and exponentially escalating heat inputs. The present paper first describes the phenomenology of
151 the boiling heat transfer in these conditions. This description is used to identify the relevant physical
152 phenomena and to develop a phenomenology of the boiling crisis. A mathematical formulation of
153 the model is then proposed and discussed using physical considerations. Lastly, the effect on boiling
154 crisis of the main experimental parameters (subcooling, mass flow rate, power exponential period) is
155 examined in the light of non-dimensional groups introduced in the model.

156 **2 Experimental observations and interpretations**

157 In this paper, we use the experimental data discussed in Kossolapov et al. [9]. Details about the
158 experimental facility, the diagnostics and the uncertainties of the experimental data can be found in
159 Ref [9]. Briefly, these experiments were conducted in a $1 \times 3 \text{ cm}^2$ rectangular cross section channel.
160 The heater is located in one of the channel side, and is made of a $2 \times 2 \text{ cm}^2$ square, 1mm-thick
161 sapphire substrate coated by a film of ITO $0.7 \mu\text{m}$ thick. The latter is placed roughly 65 hydraulic
162 diameters downstream the channel entrance to ensure a fully developed dynamic turbulent boundary

163 layer [21]. The power input is generated by Joule effect in the ITO, electrically conductive, and the
164 effective heating surface is a $1 \times 1 \text{ cm}^2$ square. The experiments were diagnosed by a high-speed IR
165 camera (2500 FPS) located behind the heater. The latter is synchronized with a high-speed video
166 camera (20000 FPS) placed front of the heater for visualization. The post processing of the IR
167 camera data, presented in [22], enables to measure the time-dependent distributions on the heating
168 wall of the temperature and the heat flux released to the water as well as their space average quantity
169 $T_w(t)$ and $q_w''(t)$.

170 **2.1 Transient boiling crisis for high Reynolds numbers and high sub-** 171 **coolings**

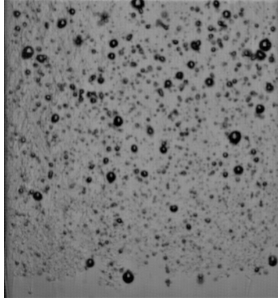
172 A large variety of tests have been conducted in order to investigate the impact on the critical heat
173 flux of several relevant parameters: flow conditions, subcooling and exponential escalation period.
174 As reported in Kossolapov et al. [9], for a high subcooling ($\Delta T_{sub} \geq 50 \text{ K}$), the heating wall is
175 homogeneously covered by numerous tiny bubbles (about $100 \mu\text{m}$ in diameter) of short life-time (less
176 than $100 \mu\text{s}$). This behavior is not taken into account in the boiling crisis models of the literature.
177 Yet, these conditions of high subcooling combined with forced flow are particularly relevant for
178 experimental nuclear reactor safety and need to be further investigated. Plus, in order to assess the
179 validity limit of the phenomenology, we decide to consider a smaller subcooling equal to 25 K. To
180 summarize, we investigate the flow boiling crisis of water at atmospheric pressure in the following
181 range:

- 182 • Power escalation period, from 5 ms to 500 ms.
- 183 • Subcooling, from 25 K to 75 K.
- 184 • Reynolds number, from 8500 to 35000.

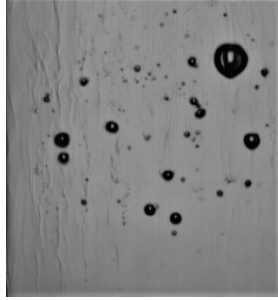
185 In Figure 1, we illustrate the transient path for such conditions with the associated transient boiling
186 curve. Pictures of the boiling process as recorded by the HSV camera, are presented for the different
187 stages of the transient boiling curve and described hereafter.

188

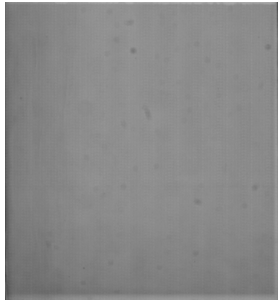
3a. FDNB (low heat flux)



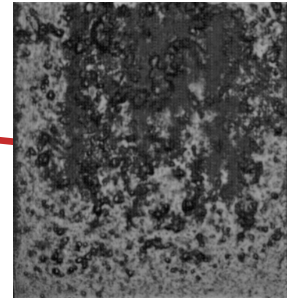
2. ONB



1. Single Phase



4. Boiling Crisis



3b. FDNB (high heat flux)

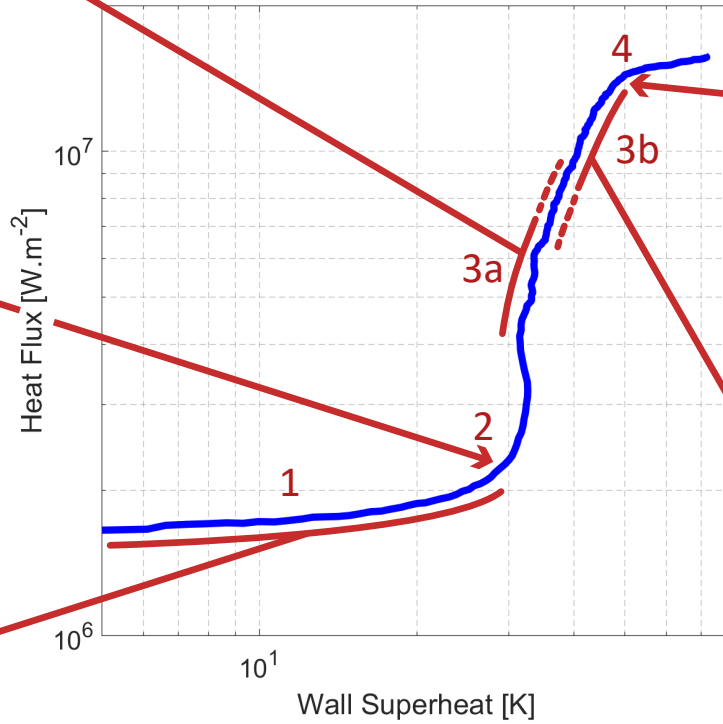
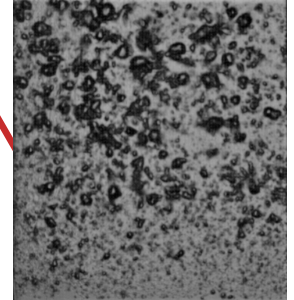


Figure 1: Illustration of the time sequence of the transient heating from single phase to the boiling crisis. HSV images illustrate the successive regimes and each square represents the whole surface of the heater (1cm x 1cm) for the case $p = 1$ bar, $\Delta T_{sub} = 75$ K, $Re = 35000$, $\tau = 50$ ms.

189

1. Single-phase regime

190

Single phase heat transfer is realized in the subcooled water and results from the cumulative actions of the turbulent convection processes and the transient heat conduction. Further information on this regime may be found in the recent work of Chavagnat et al. [23]. Nevertheless, the heat flux to water is still low at this stage (point 1 in Figure 1).

194

195

2. Onset of Nucleate Boiling and Overshoot

196

Boiling incipience occurs once the temperature at the heated wall is large enough to activate the nucleation sites. A rapid transient heat input at high subcooling often leads to a temperature overshoot (OV). This phenomenon is widely reported in the literature (Rosenthal [24], Sakurai & Shiotsu [25, 26], Su et. al. [27, 28]). One may observe on the boiling curve a wall superheat higher than in steady-state conditions. In figure 1, the OV is slightly visible as the transient is relatively slow.

200

201 This overshoot effect is a temporary process. It is linked to the time lag required for activation of
202 the nucleation sites. It increases with the heat generation rate.

203

204 **3. Fully Developed Nucleate Boiling**

205 After the overshoot, most of the nucleation sites are activated and the wall appears to be homoge-
206 neously covered by bubbles. As reported in Kossolapov et al. [9], *e.g.* in Fig. 6 of the reference, the
207 bubble diameter decreases with the increase of the subcooling and can be as small as about $100 \mu m$.
208 Moreover, our HSV analysis shows that, in high subcooling conditions, have a short lifetime, about
209 $100 \mu s$. Qualitatively, this can be explained considering that bubbles grow up to a small diameter
210 then rapidly collapse due to the cold surrounding water. More interestingly, the HSV reveals a pulsat-
211 ing bubble behavior. Bubbles continuously grow and collapse with a frequency greater than 10 kHz.
212 In addition, videos show that bubbles hardly lift-off their nucleation site but remain confined at the
213 vicinity of the wall. It is worth to note that for $\Delta T_{sub} = 25 K$, condition used to assess the validity
214 limit, this mechanism is less pronounced, bubbles have a longer lifetime, about a few milliseconds,
215 and have a width up to $3 mm$. Bubbles with such dimensions are not necessarily spherical. This
216 process is observed during the entire Fully Developed Nucleate Boiling (FDNB) regime, the density
217 of bubbles increasing with the heat flux. This evolution is illustrated by HSV images in figure 1 where
218 the density of bubbles is seen to increase from point 3a to 3b. The period of the power escalation
219 does not qualitatively change this behavior.

220

221 **4. Boiling Crisis**

222 As the heat flux increases, bubbles become more and more numerous on the wall. Local and intermit-
223 tent dry spots occur due to lateral coalescence of some neighboring bubbles. These dry spots may be
224 reversible, *i.e.* the wall can be rewetted. However, as the heat transferred from the heating surface
225 to the fluid increases, the lateral coalescence of the neighboring bubbles leads to the formation of
226 irreversible dry spots, *i.e.* to the boiling crisis (point 4 in Figure 1). According to observations made
227 from both HSV and IR camera, the spatio-temporal dynamics of the dry spots changes with the time
228 period τ . For fast transients, dry spots appear uniformly on the entire heating wall. Conversely, for
229 longer transients, dry spots seem to preferentially appear downstream the heating wall, as illustrated
230 by point 4 in Figure 1. This observation will be interpreted in section 4.3 in regard of the model
231 developed in the present work. The transition between fast and slow transients mainly depends on
232 the imposed flow regime, occurring at about 20 ms for high flow rate and 100 ms for low flow rate.

234 2.2 Physical description of the model

235 Considering the observations reported in the former section, we propose to model the boiling cri-
 236 sis by the following mechanism: boiling crisis is triggered when bubbles generated at the wall can
 237 no longer condense in the surrounding liquid, then coalesce laterally generating irreversible dry-
 238 spots. Indeed, under conditions of high subcooling and strong forced convection, the observations
 239 reveal that each bubble grows, then condenses in the surrounding cold liquid and finally disappears.
 240 Subsequently, other bubbles are generated at the wall and the process is repeated. One observes
 241 Nucleation and Condensation Cycles (NCC) happening at high frequency (about 10 kHz). These
 242 NCCs contribute to an efficient heat transfer from the wall to the liquid. Heat released by the
 243 condensing bubbles contribute to increase the sensible heat of the liquid. When the liquid reaches
 244 the saturation temperature, nucleated bubbles cannot condense anymore triggering the boiling crisis.

245

246 We recall that the investigated conditions are high subcooling and strong forced flow (high
 247 Reynolds number). Consequently, the bubbles remain small and constrained at the wall by the
 248 shear stress as detailed in section 2.1. Then most of the physical phenomena relevant to this inves-
 249 tigation will take place in a small layer of fluid at the vicinity of the wall. This is where the NCCs
 250 take place: it includes the bubbles and the adjacent liquid in which they condense. This layer will
 251 be hereafter called the "mantle" and its thickness will be denoted δ . Besides, bubble growth and
 252 collapse induce a highly efficient mixing which contributes to homogenize the temperature of the
 253 liquid in the mantle thickness. Considering its definition and the phenomena involved within it, the
 254 mantle is a different concept than a conductive sublayer or a classic thermal boundary layer. Once
 255 the liquid in the mantle reaches the saturation temperature, the bubbles can no longer condense.
 256 This condition will then be considered as a quantitative criterion for the triggering of the boiling
 257 crisis. This scenario is schematically summarized in Figure 2 and sequentially described hereafter.

258

259 The transient process starts with single-phase forced convection until the first bubble appears
 260 on the heated wall (ONB). During FDNB, bubbles have a pulsating behavior. They are small and
 261 promptly collapse after their nucleation leading to high frequency Nucleation and Condensation Cy-
 262 cles (NCC). These effects are only perceptible near the wall. The model postulates that the highly

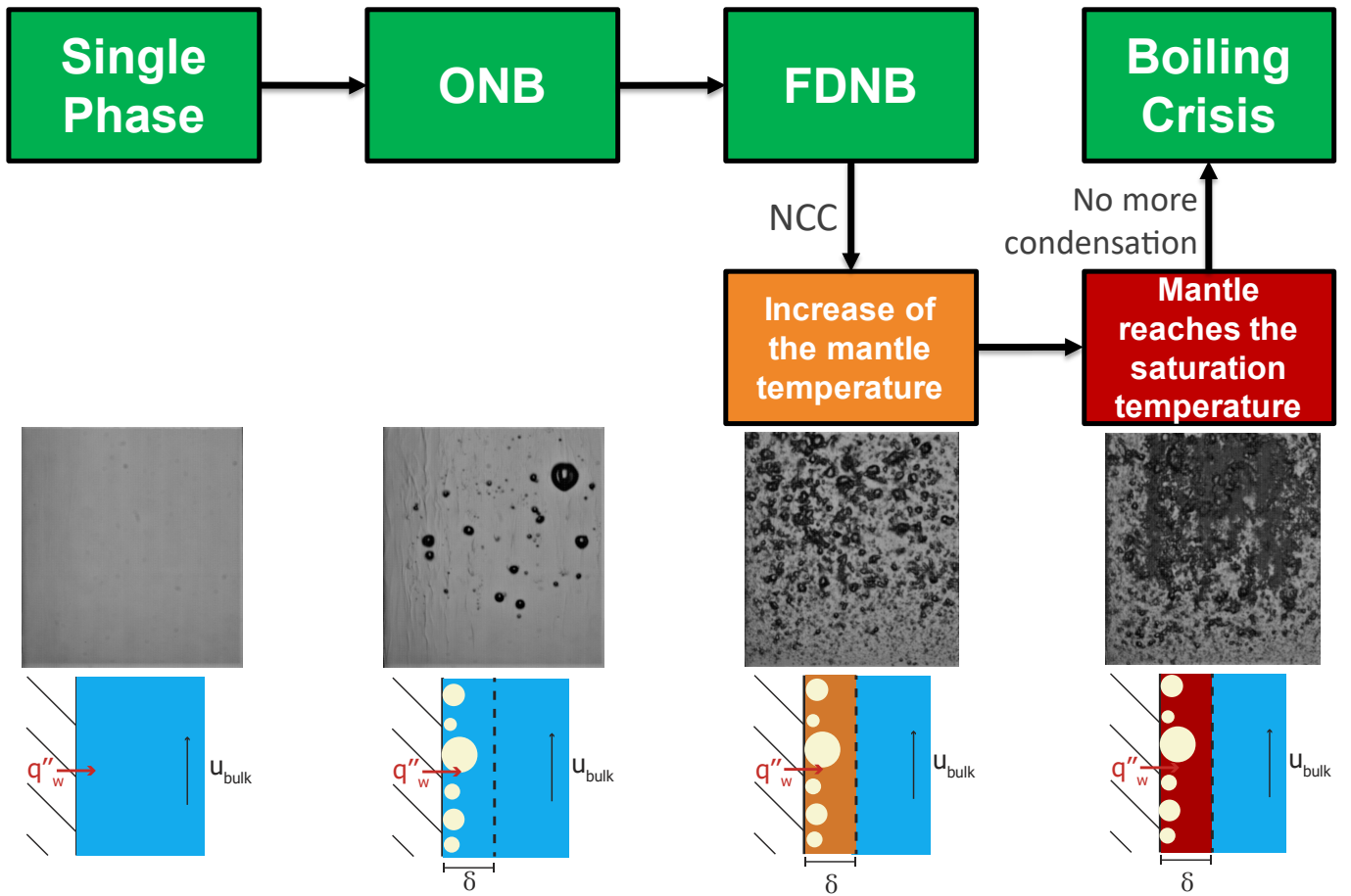


Figure 2: Interpretation of successive events leading to boiling crisis in conditions of high subcooling and strong forced convection. Front backlit shadowgraphy images correspond to the case $p = 1$ bar, $\Delta T_{sub} = 75$ K, $Re = 35000$, $\tau = 50$ ms and represent the entire heating surface (1 cm x 1 cm). The bottom schemas illustrate the model considerations with a side view.

263 efficient mixing induced by NCCs leads to the homogenization of the energy throughout the thickness
 264 of the mantle, *i.e.* in the direction normal to the wall. This thickness δ is assumed to be constant
 265 throughout the transient process. This assumption is statistically reasonable considering that the
 266 mantle is defined as the region dominated by the influence of pulsating bubbles and the size of these
 267 bubbles does not significantly change during FDNB (see pictures 3a, 3b and 4 in Figure 1). A second
 268 major assumption considers that the thickness δ is also assumed to be uniform alongside the heater
 269 in a first approximation to avoid dispensable fitting constants.

270

271 During FDNB, the energy stored in the mantle results from the competition between the heat
 272 input supplied from the wall and the cooling processes due to forced convection (that will be detailed
 273 in section 4.3). Because of the exponential nature of the heat input, the energy density rises in time.
 274 Once it reaches the critical value, *i.e.* when the local subcooling becomes null, bubbles generated at
 275 the wall can no longer condense. They coalesce triggering the formation of irreversible vapor pockets,
 276 which next results in a boiling crisis.

278 The model describes the exchanges between two homogeneous zones presented in Figure 2:

- 279 • **The mantle** of thickness δ , where the energy density is homogenized by the NCCs. This
280 thickness is assumed to be small compared to the channel width.
- 281 • **The bulk**, where cold liquid water flows at a high Reynolds number and high subcooling. The
282 bulk temperature is considered as being unmodified during the transient heating process.

283 The energy density homogeneity in the mantle is a reasonable approximation. Indeed, during FDNB,
284 the high speed videos revealed the small size of the bubbles, around $100 \mu m$, which is two orders of
285 magnitude smaller than the width of the channel. Therefore, we expect the mantle thickness to have
286 the order of magnitude of the bubble diameter and small compared to the channel width. By their
287 pulsating behavior, the generated bubbles would then mix the fluid in mantle and homogenize its
288 temperature. Besides, the energy density is considered to be constant in the direction of the width
289 of the heater.

290

291 This model relies on some input data which are experimental quantities : *i*) thermal and hydraulic
292 operating conditions (pressure, subcooling, mass flow rate, time period for the exponential rise), *ii*)
293 the measured space-averaged heat flux transferred to the water $q_w''(t)$.

294

295 This approach is akin to the model of Weisman and Pei [29] who proposed an interaction between
296 two distinct domains due to turbulent velocity fluctuations. However, Weisman and Pei considered
297 the exchange of bubbles whereas our model proposes to study an exchange of energy. Moreover,
298 our model is also akin to the critical enthalpy approach proposed by Tong [30] who conducted an
299 enthalpy balance in the close vicinity of the wall and proposed a criterion on the enthalpy value.
300 However, the lack of physical modeling of the various terms of the enthalpy balance and the stated
301 critical enthalpy led Tong to use numerous correlations on experimental data. Moreover, these two
302 approaches [30, 29] were developed to investigate steady heating situations. The literature has widely
303 reported (*e.g.* [7, 8, 9]) that when the power escalation period is small enough, the value of CHF
304 differs from its value for longer period and depends on the power escalation period, bringing to
305 light transient effects. Failing to predict whether a case can be considered as quasi steady-state or
306 period-dependent, it is then necessary to develop a model considering a time-dependent mechanism
307 to describe the transient boiling crisis.

308 **3 Mathematical formulation**

309 **3.1 Criterion for the Boiling Crisis**

310 As stated above, the criterion associated with the triggering of boiling crisis under the considered
311 conditions is when energetically, an elementary volume of liquid water (dV) in the mantle is heated
312 from the initial subcooled temperature to saturation, corresponding to an energy rise of $c_p \rho_l \Delta T_{sub} dV$.
313 The critical energy density rise E'''_{cr} will then be defined by:

$$E'''_{cr} = \rho_l c_p \Delta T_{sub} \quad (1)$$

314 When the local energy density rise in the mantle reaches this critical value E'''_{cr} , the next generation
315 of bubbles will no longer condense. These bubbles will instead laterally merge triggering the boiling
316 crisis. The critical energy density rise E'''_{cr} is thus a suitable criterion to characterize the boiling crisis.

317
318 It is worth to note that this criterion does not involve directly the latent heat. We have shown
319 that under conditions of interest, bubbles have a short lifetime: less than $100 \mu s$. This is 2 to 5 orders
320 of magnitude smaller than the period of the exponential power excursion which is the characteristic
321 time scale of the investigated phenomenon. As stated in section 2.2, the model assumes that the
322 energy required to generate a bubble, *i.e.* involving the latent heat, is then entirely released to the
323 adjacent liquid in the mantle, *i.e.* converted to sensible heat. In other words, the contribution of
324 the latent heat is mechanistically considered as an intermediate step which efficiently transfers the
325 heat from the wall to the liquid phase. This temporary process has a time scale much smaller than
326 the time scale of the investigated phenomenon, *i.e.* the power escalation period τ . Therefore, it is
327 reasonable not to include the latent heat in this criterion for the proposed model.

328
329 In the following, we aim to establish an equation on the local energy density rise describing its
330 evolution during the transient heating.

331 **3.2 Governing equations of the mantle**

332 To describe mathematically the evolution of the local energy density, one needs to establish an energy
333 balance in the mantle. Let us consider the mantle region of thickness δ which separates the wall from
334 the bulk fluid as depicted in Figure 3. The assumptions discussed in section 2.2 consider that the

335 physical quantities do not depend on the variable z . The successive nucleation-condensation cycles
 336 of the bubbles induce homogenization in the transverse direction y inside the mantle. The heat flux
 337 $q''_w(t)$ supplied from the wall to the fluid contributes to the bubble generation. The energy of the
 338 fluid in the mantle increases gradually due to heat released by NCCs. Conversely, part of this energy
 339 is lost due to two contributions. The first one is the advection in the streamwise direction due to
 340 the vertical velocity component (u_m in Figure 3). The second one is the heat exchange between the
 341 mantle and the bulk due to turbulent velocity fluctuations (v_m in Figure 3). These exchanges will
 342 be discussed in section 3.3.

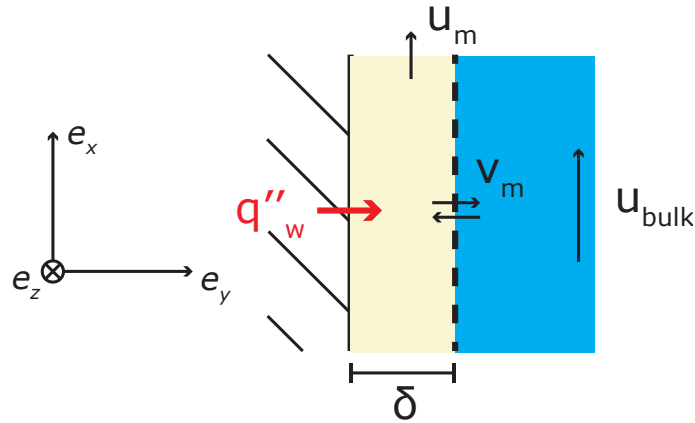


Figure 3: Schematic description of the mantle ($y \in [0, \delta]$)

343 An elementary control volume $\sigma(x)$ is defined as an element of volume $dx \delta dz$ at the vicinity of the
 344 wall, between x and $x + dx$. In the y -direction, the length of the elementary volume is δ because we
 345 consider the entire mantle thickness. This definition is illustrated in Figure 4.

346

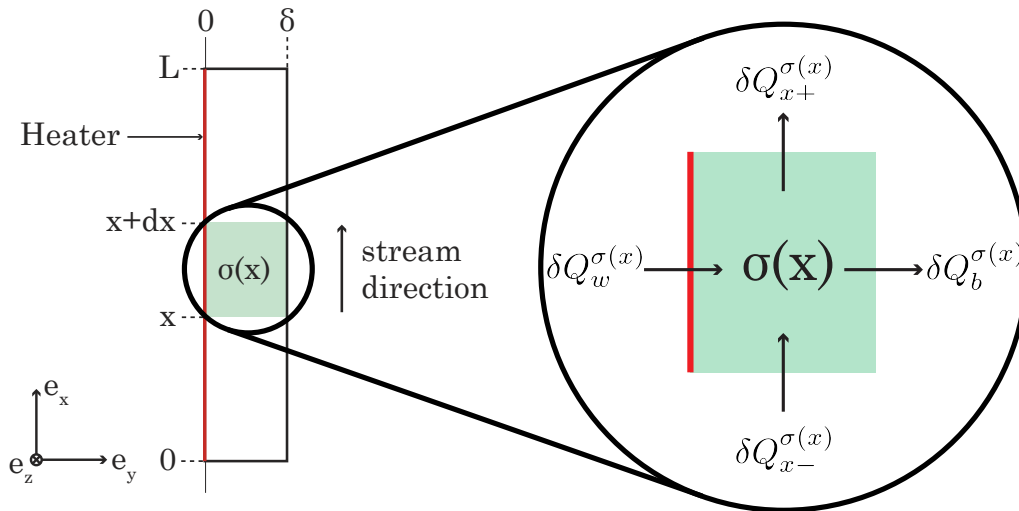


Figure 4: Description of the entire system considering the total length L of the heater and the exchanges of the elementary system $\sigma(x)$ used for the energy balance.

347 The considered system $\sigma(x)$ has a total energy $E_\sigma(x, t)$ [J] carried by the fluid within it. By con-
 348 sidering the bulk energy density E_0''' [$J.m^{-3}$] and the energy density rise $E'''(x, t)$ [$J.m^{-3}$], one can
 349 define:

$$E_\sigma(x, t) = \left(E'''(x, t) + E_0''' \right) dx \delta dz \quad (2)$$

350 The variation of energy dE_σ is written:

$$\begin{aligned} dE_\sigma &= E_\sigma(x, t + dt) - E_\sigma(x, t) \\ &= (E'''(x, t + dt) - E'''(x, t)) dx \delta dz \end{aligned}$$

351 thus

$$dE_\sigma = \frac{\partial E'''}{\partial t} dx \delta dz dt \quad (3)$$

352 The exchange of energy at the interface is written:

$$dE_\sigma = \delta Q_w - \delta Q_{x+}^{\sigma(x)} + \delta Q_{x-}^{\sigma(x)} - \delta Q_b^{\sigma(x)} \quad (4)$$

353 where (see Figure 4):

- 354 • δQ_w is the heat coming from the wall.
- 355 • $\delta Q_{x-}^{\sigma(x)}$ is the heat coming by advection from $\sigma(x - dx)$.
- 356 • $\delta Q_{x+}^{\sigma(x)}$ is the heat leaving the control volume by advection to $\sigma(x + dx)$.
- 357 • $\delta Q_b^{\sigma(x)}$ is the heat transferred at the interface mantle-bulk (at a distance $y = \delta$ from the wall).

358 the expressions of the different terms are:

$$\delta Q_w = q_w''(t) dx dz dt \quad (5)$$

$$\delta Q_{x-}^{\sigma(x)} = u_m(E_0''' + E'''(x, t)) \delta dz dt \quad (6)$$

$$\delta Q_{x+}^{\sigma(x)} = u_m(E_0''' + E'''(x + dx, t)) \delta dz dt \quad (7)$$

$$\delta Q_b^{\sigma(x)} = q_b''(x, t) dx dz dt = v_m E'''(x, t) dx dz dt \quad (8)$$

359 with $q_b''(x, t) = v_m E'''(x, t)$ the net heat flux transferred at the interface mantle-bulk. The demon-
 360 stration of its expression will be presented in section 3.3. These expressions substituted in equation
 361 4 give after simplification:

$$\frac{\partial E'''}{\partial t} + u_m \frac{\partial E'''}{\partial x} + \frac{v_m}{\delta} E''' = \frac{q_w''}{\delta} \quad (9)$$

362 In the present situation with an established forced convection and with high heat fluxes supplied
 363 from the wall, the following terms may be neglected: kinetic, gravitational, viscous dissipation and
 364 pressure effects.

365

366 Equation (9) can be transformed into a non-dimensional expression. The dimensionless volumetric
 367 energy density rise E^* is defined with respect to the critical energy: $E^* = E''' / E_{cr}'''$. The length of
 368 the heater, L , is used to set a normalized form of the variable x : $x^* = x/L$. Time period τ of the
 369 exponential rise is used to define a normalized time: $t^* = t/\tau$. Substituting these three quantities in
 370 Eq. 9, we obtain:

$$\frac{\partial E^*}{\partial t^*} + N_x \frac{\partial E^*}{\partial x^*} + N_y E^* = \frac{\tau}{E_{cr}'''} q_w'' \quad (10)$$

371 where N_x and N_y are two non-dimensional groups defined as:

$$N_x = \frac{u_m \tau}{L} \quad N_y = \frac{v_m \tau}{\delta} \quad (11)$$

372 A well posed mathematical problem requires for this first-order partial differential equation to
 373 have initial and boundary conditions. At time $t^* = 0$, the temperature of the fluid is uniform in
 374 the whole channel, equals to the inlet temperature : $E^*(x^*, 0) = 0$. The fluid entering the heated
 375 section, at $t^* = 0$, has a temperature equal to the bulk temperature which remains the same during
 376 the whole transient heating process. This condition reads $E^*(0, t) = 0, \quad \forall t > 0$. To fully formulate
 377 the mathematical problem, we still need to define the two velocities u_m and v_m characterizing the

378 cooling process induced by the forced flow.

379 **3.3 Heat transport induced by the flow**

380 The velocity in the streamwise direction is $u(\vec{x}, t) = U(y) + u'(\vec{x}, t)$. Neglecting the fluctuating
381 component $u'(\vec{x}, t)$, this velocity will be approximated by its mean component $U(y)$, this latter being
382 given by the law of the wall for a turbulent channel flow. As strong velocity gradients are present
383 near the wall, a spatial average along the mantle thickness will also be considered:

$$u_m(\delta) = \frac{1}{\delta} \int_0^\delta U(y) dy \quad (12)$$

384 Once the bubbles are generated at the wall, the mean velocity profile is perturbed from the law of
385 the wall. Nonetheless, its use as a first approximation to compute u_m is reasonable. The latter is
386 a space averaged velocity within the thickness δ which is greater than the diameter of the bubbles,
387 implying that most of the area accounted for to compute the mean velocity is sparsely influenced by
388 the bubbles.

389
390 Moreover, as described above, the bubbles are small, quasi-spherical and pulsate at high frequency
391 without having time to slip over the surface. This leads to think that these flow perturbations do not
392 influence the streamwise average flow as the growth and collapse would be achieved symmetrically
393 compared to the center of a bubble and as the period of the pulsation is small compared to the char-
394 acteristic time period of the experiment (τ). This growth and collapse behavior however influences
395 the instantaneous flow contributing to the mantle mixing. Finally, bubbles are confined in close
396 vicinity of the wall where the velocity is strongly reduced due to the viscosity of water. Therefore,
397 most of the weight U taken into account by the calculation of the mean velocity u_m is taken where
398 the fluid is in single-phase liquid.

399
400 Then, one has to describe the heat exchange between the mantle and the bulk due to turbulence
401 in the y direction. The advection at the interface by the turbulent velocity fluctuations is taken into
402 account by a characteristic velocity v_m . Let us first recall the usual definitions for the quantities used
403 in the description of turbulent flows.

404 - u^* is the wall shear velocity calculated with the friction factor, using Blasius ($Re < 30,000$) and
405 McAdams ($Re > 30,000$) correlations as suggested in [31] (see chapter 9, section I-C (p.379)),

406 - $\delta_\nu = \nu/u^*$ is the viscous sublayer unit, with ν the kinematic viscosity of water.

407 - $Re_\tau = u^*e/\nu$ is the wall Reynolds number where e is the channel half width.

408 The corresponding values of these quantities under the investigated conditions are presented in Ta-

409 ble 1. Hereafter, we will use the following definitions: $U^+ = U/u^*$ for the dimensionless velocity and

410 $Y^+ = y/\delta_\nu$ for the normalized distance to the wall.

411

Re [-]	ΔT_{sub} [K]	Re_τ [-]	δ_ν [μm]	u^* [$cm.s^{-1}$]
8500	50	182	28	2.0
13500	25	272	18	2.1
25000	25	467	11	3.6
	50			5.2
	75			8.4
35000	25	622	8.0	4.8
	50			6.9
	75			11

412

413 Table 1: Turbulent flow characteristics for the considered conditions of [9] and for the present channel geometry. $Re = \frac{GD_h}{\mu}$ with G the mass flux, D_h the hydraulic diameter and μ the dynamic viscosity.

414 As featured in section 3.2, the heat exchanges between the mantle and the bulk are due to

415 the transverse turbulent velocity fluctuations. Let us consider a given transverse turbulent velocity

416 fluctuation v' , the elementary transfer of heat at the mantle-bulk interface dq_b'' is given by :

$$dq_b''(v') = \begin{cases} E_0''' v' P(v') dv' & \forall v' < 0 \\ (E_0''' + E''') v' P(v') dv' & \forall v' > 0 \end{cases} \quad (13)$$

where $P(v')$ is the probability density function (PDF) of the transverse velocity component v' . As illustrated in Figure 5, the first line describes a transport of cold bulk water towards the mantle and the second one describes the heated water leaving the mantle to the bulk. In order to have the net heat transport, all the possible velocity fluctuations weighted with their probability must be taken

into account. This results to the following integral:

$$q_b'' = \int_{-\infty}^{+\infty} dq_b''(v') \quad (14)$$

$$= \int_{-\infty}^0 E_0''' v' P(v') dv' + \int_0^{+\infty} (E_0''' + E''') v' P(v') dv' \quad (15)$$

$$= E_0''' \int_{-\infty}^0 v' P(v') dv' + (E_0''' + E''') \int_0^{+\infty} v' P(v') dv' \quad (16)$$

$$= E_0''' \int_{-\infty}^{+\infty} v' P(v') dv' + E''' \int_0^{+\infty} v' P(v') dv' \quad (17)$$

417 v' being a turbulent velocity fluctuation,

$$\int_{-\infty}^{+\infty} v' P(v') dv' = \langle v' \rangle = 0 \quad (18)$$

418 the first term of equation 17 is then null and the net heat flux at the interface mantle-bulk is given

419 by $q_b'' = v_m E'''$ with:

$$v_m = \int_0^{+\infty} v' P(v') dv' \quad (19)$$

420 With v_m the characteristic velocity of the transverse turbulent velocity fluctuation. This characteris-

421 tic velocity is also the expected value of the positive velocity fluctuation: $v_m = \mathbb{E}(v' | \mathbb{R}^+)$. Besides,

422 decomposing v_m enables a better understanding of its two contributions: the cold bulk water inflow

423 and the warmed water outflow. Indeed, as $\langle v' \rangle = 0$, $\int_{-\infty}^0 v' P(v') dv' = - \int_0^{+\infty} v' P(v') dv' = -v_m$ and

424 one can rewrite equation 16 as:

$$q_b'' = \overbrace{v_m(E_0''' + E''')}^{\text{Warmed mantle water outflow}} - \underbrace{v_m E_0'''}_{\text{Cold bulk water inflow}} \quad (20)$$

425 which is illustrated in Figure 5. Noteworthy, we model the heat exchange in the normal direction by

426 an interaction between two homogeneous media in term of temperature, the mantle and the bulk.

427 Consequently, this choice of modeling does not involve thermal turbulent fluctuations terms such as

428 $\langle v' T' \rangle$.

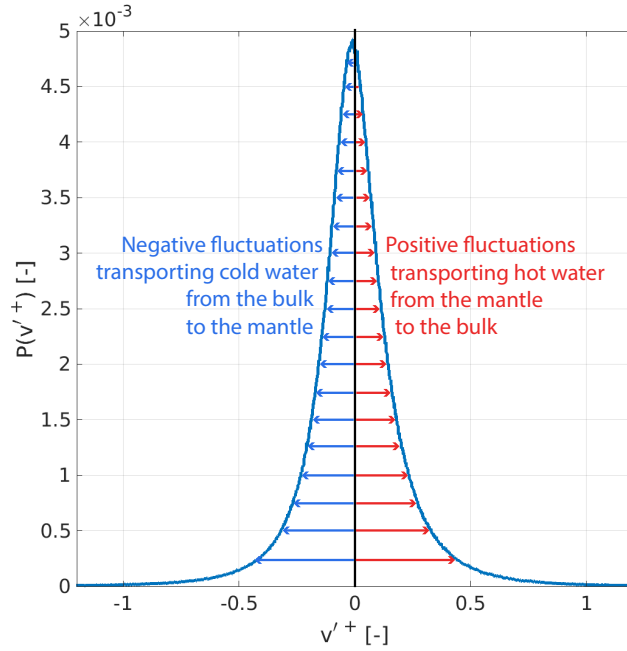


Figure 5: Schematic description of the velocity fluctuation contributions at the interface mantle-bulk. The PDF is extracted from the data of [32] with $Re_\tau = 1000$ at $y^+ = 10$. Noteworthy, the asymmetry reflects the anisotropy of the near-wall flow, while the property $\langle v'^+ \rangle = 0$ remains verified.

429 The formulation of the characteristic velocity v_m is akin to the characteristic velocity defined by
 430 Weisman & Pei [29] and Pasamehmetoglu [20]. In their case, they aim to determine the velocity of
 431 liquid inflowing a layer (the bubbly layer for Weisman and Pei and the macrolayer for Pasamehme-
 432 toglu) at low subcooling where vapor effectively leaves the denominated zone, characterized by a
 433 vapor ejection velocity. In our case, bubbles do not depart from the wall because of the high sub-
 434 cooling. Thus, at a distance greater than the bubble diameter, in particular at a distance δ from
 435 the wall, there is no vapor mass flux escaping. Moreover, bubbles have a pulsating behavior. In
 436 our model, we chose to assume that the velocity field generated by the bubble growth is dampened
 437 by the bubble collapse and that these velocities have no significant influence on the exchanges at
 438 the interface mantle-bulk. For these reasons, a null vapor ejection velocity appears to be a quite
 439 reasonable approximation in our case and thus our proposed expression of v_m does not contradict
 440 theirs. However, the present expression establishment and its use in Equation 10 takes into account
 441 the whole distribution of the transverse turbulent velocity fluctuations, and not only a part as in
 442 [29] and [20], improving the use of this physical quantity. Plus, these authors make use of assumed
 443 expressions of the PDF $P(v')$, Gaussian for Weisman and Pei and Hyperbolic for Pasamehmetoglu,
 444 whose accuracy is not quantitatively assessed.

445

446 In order to compute v_m , one needs to know of $P(v')$. This latter function can be obtained by

447 analyzing Direct Numerical Simulation (DNS) data or by making analytic assumptions on the func-
448 tion $P(v')$. In the present paper, we choose to use DNS data as discussed shortly hereafter. DNS
449 simulations were performed by Moser et al. [33] and Graham et al. [32] to study turbulent flows
450 inside a rectangular channel. We use the latter to compute the value of v_m as a function of different
451 value of Re_τ which enables interpolations to each specific experimental conditions. The detail of the
452 process is developed in the appendix A.

453

454 In their calculation, Weisman and Pei assumed that $P(v')$ has a Gaussian distribution every-
455 where in the domain. Pasamehmetoglu assumed a hyperbolic distribution, $P(v') \propto (1/v')^n$ with
456 n , an adjustable empirical coefficient equal to 4. However, this choice seems to be the result of an
457 empirical fitting. On the other side, assuming a Gaussian distribution could be relevant in the bulk.
458 However, this is no longer true near the wall as anisotropy deviates the probability density function
459 from a Gaussian distribution. This analysis, detailed in Appendix A, is illustrated in Figure 6b where
460 we plot the relative discrepancy between each resulting v_m^+ , between our methodology and the one
461 proposed by Weisman & Pei. For our working conditions, *i.e.* with a Reynolds number up to about
462 600 (see Table 1), the difference can be as high as 16 % for the near-wall flows. However, the error
463 can be as high as 50% difference when the wall Reynolds number reaches higher values relevant for
464 extended applications. Based on this analysis, we decided to use directly PDFs obtained by DNS
465 simulations to compute v_m .

466

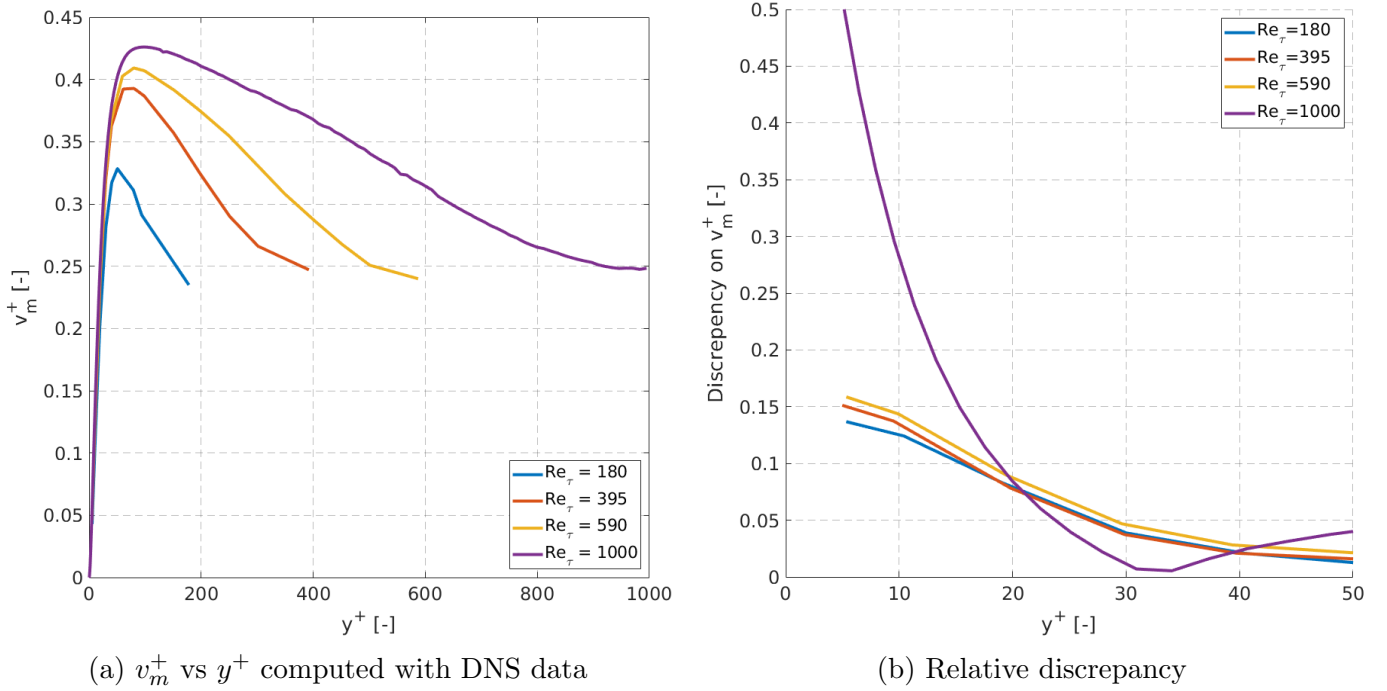


Figure 6: Dimensionless velocity v_m^+ as a function of the dimensionless normal coordinate y^+ calculated for $Re_\tau = 180, 395, 590, 1000$ with DNS data of Moser et al. [33] and Graham et al. [32]. Relative discrepancies between the calculation of v_m^+ using PDF data and the Gaussian distribution assumption are presented.

467 The current calculation of v_m uses single-phase DNS data. In fact, the growth and collapse
 468 of bubbles at the wall induces supplementary turbulent velocity fluctuations. Particularly, they
 469 would most likely increase the value of v_m : the growth adding positive fluctuations and the collapse
 470 negative ones, v_m defined as the integration of the fluctuation in a direction would necessarily increase.
 471 However, quantifying the influence of the bubble-induced fluctuations is currently out of range.
 472 Consequently, in the present model, we assume that the fluctuations induced by the bubbles do not
 473 impact the velocity v_m .

474 3.4 Model Implementation and Output

475 We will now discuss the various parameters involved in Equation 9:

- 476 • $q_w''(t)$ is the heat flux released from the wall to the fluid. This time-function is known from
 477 experimental data. In all experiments the heat flux distribution on the boiling surface was
 478 spatially uniform until the boiling crisis. Therefore, a space-averaged value of heat flux is used
 479 as an input to our model.
- 480 • the characteristic velocities u_m and v_m have been presented in section 3.3. Both quantities
 481 depend on the operating conditions (pressure, bulk temperature, mass flow rate) and also on

482 the mantle thickness δ .

- 483 • The mantle thickness δ is *a priori* unknown.

484 The present model assumes that boiling crisis happens when the condition $E'''(x, t_{CHF}) = E'''_{cr}$ is
485 reached. It is used to estimate the *a priori* unknown quantity δ .

486
487 In order to assess the thickness δ , a guess-estimate approach is realized as described in the
488 following and illustrated in the flowchart in Figure 7. To do so, we use the time-dependent infrared
489 thermography information recorded for the experimental CHF investigation of Kossolapov et al. [9].
490 Particularly, for each test, we extracted two quantities and used them as input in the algorithm:
491 the time of the boiling crisis t_{CHF} , and the recorded space-averaged heat flux $q''_w(t)$ (time t ranging
492 between zero and t_{CHF}). A first value of δ is chosen and Eq.(10) is then integrated with an explicit
493 forward Euler method from $t = 0$ to $t = t_{CHF}$. If the volumetric energy density rise at time t_{CHF}
494 differs from the critical value, the δ value is considered wrong. Another value is fixed and the process
495 is repeated again. The correct value δ is obtained when convergence is achieved:

$$496 \quad \left| \max_{x^* \in [0,1]} (E^*(x^*, t_{CHF}^*)) - 1 \right| < \varepsilon \quad (21)$$

496 with ε , the criterion of convergence. As in this investigation, the heat flux input is uniform
497 along the x -direction, E^* is a monotonically increasing function in the streamwise direction and the
498 maximum is then located at the extremity, downstream the heating wall, *i.e.* at $x^* = 1$. Plus a
499 criterion of convergence of 10^{-3} has been selected on our case.

500 It is worth to note that this quantity δ is the result of this algorithm and not the outcome of
501 a measurement. The measurement of such a quantity is currently not possible. Indeed, one would
502 need to quantitatively and finely measure the temperature field close to the heating wall. However,
503 due to the thin mantle thicknesses involved, the turbulent thermal flow and the numerous bubbles
504 located at the wall, this measurement is currently impossible.

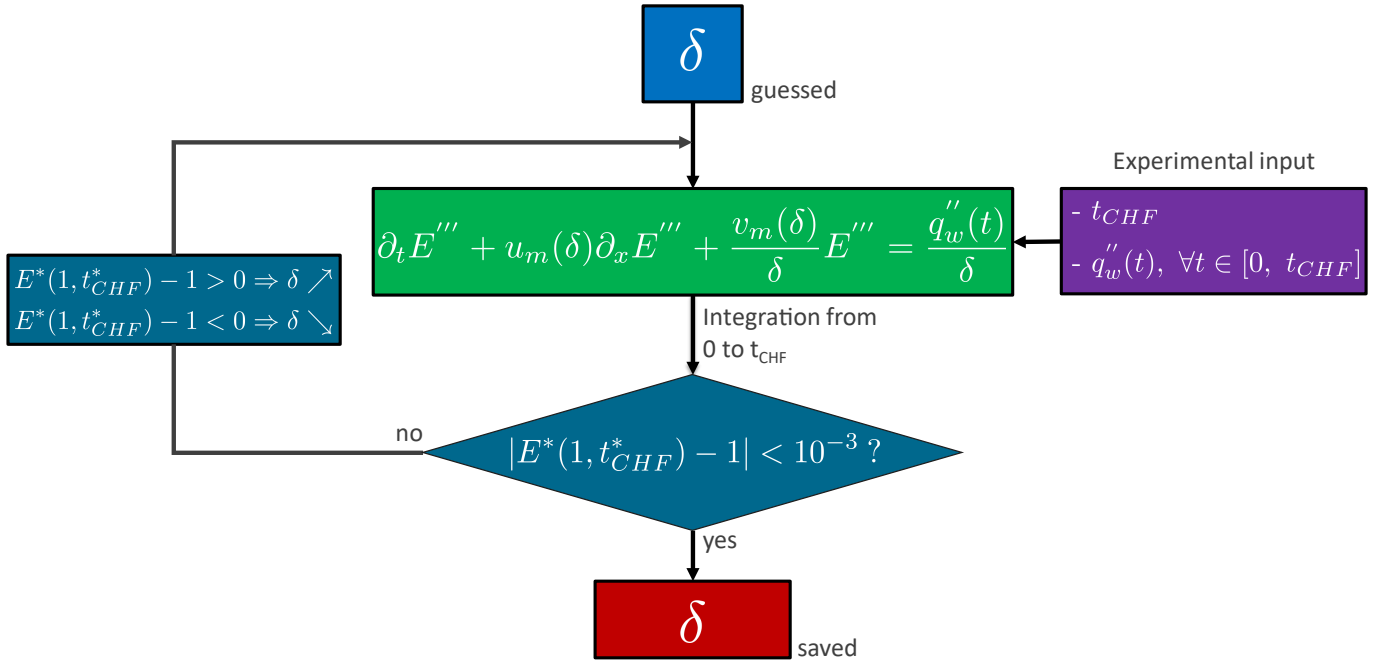


Figure 7: Schematic description of the guess-estimate algorithm allowing for the determination of the mantle thickness δ for a given experimental run.

505 4 Results and physical discussion

506 4.1 Evaluation of the mantle thickness

507 4.1.1 Experimental results and correlation

Equation (10) is solved for the considered set of experimental conditions. The obtained values for the thickness δ are plotted as a function of the time period τ in Figure 8a. The values can also be normalized using the length $\delta_\nu = \nu/u^*$ which is the relevant turbulent length scale in the transverse direction (Figure 8b):

$$\delta^+ = \frac{\delta}{\delta_\nu}$$

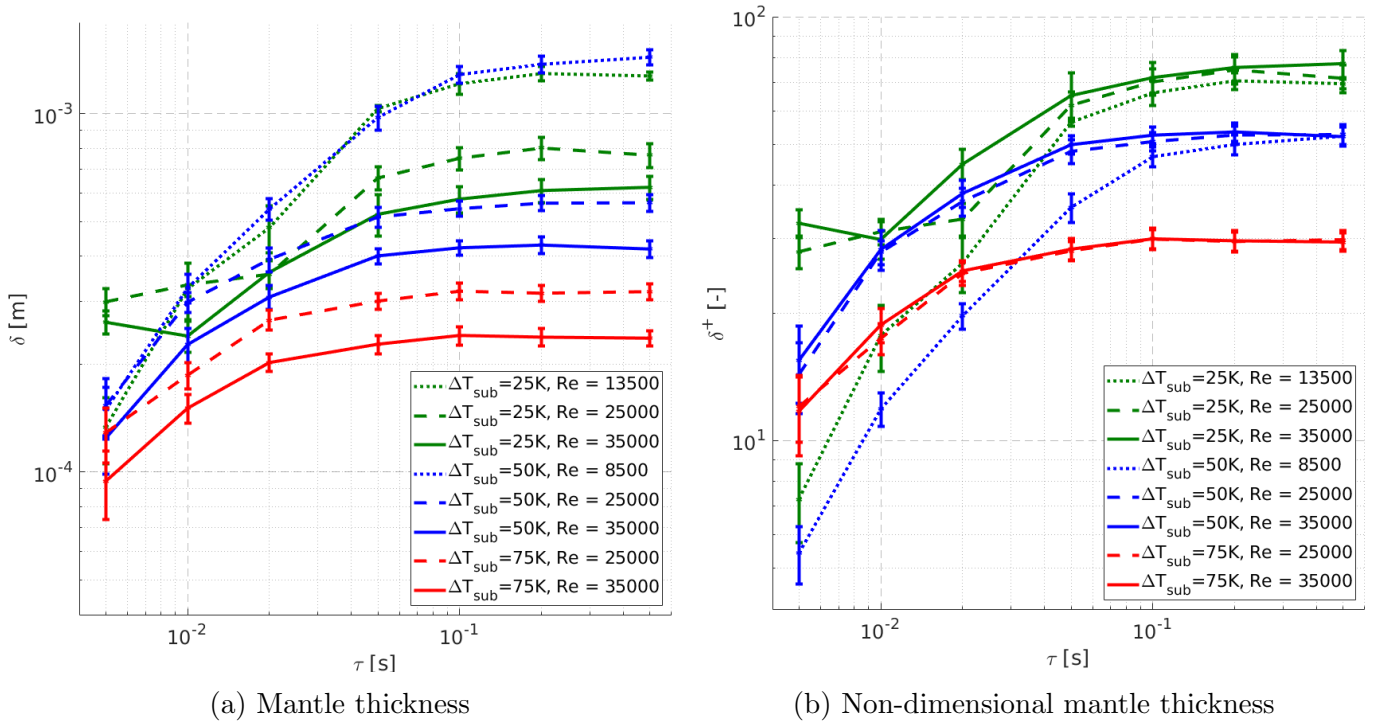


Figure 8: Thickness of the mantle δ [m] and its dimensionless form δ^+ [-] as a function of the excursion period τ [s] for the eight operating conditions.

508 Each of the eight curves plotted in Figure 8 consists in seven points (5, 10, 20, 50, 100, 200, 500 ms).
 509 For each point, three runs were conducted. Therefore, the results presented in Figure 8 are derived
 510 from 168 measurement points. The considerations to compute the uncertainty on δ are detailed in
 511 appendix B.

512
 513 The mantle thickness is presented in Figure 8a. It goes from 100 μm for the short periods and
 514 high Reynolds numbers to 2 mm for long periods and low Reynolds numbers. For the high subcooling
 515 degrees (50 K and 75 K), these values are slightly larger (short periods) or significantly larger
 516 (long periods) than the bubble diameters, *i.e.* that supports the assumption presented in section 3.3.
 517 However, for 25 K of subcooling, the mantle thickness takes values smaller than the bubble diameters
 518 (discussed in section 4.1.2). One can note that δ increases with the period τ until a plateau which
 519 is reached for τ larger than 100 ms. This increasing trend is regular for most of the test, except
 520 for the ones with $\Delta T_{sub} = 25K$. The value taken by this plateau decreases with the increase of the
 521 subcooling and the Reynolds number, but no quantitative regularity is observed. However, when
 522 the mantle thickness is normalized by the length δ_ν (Figure 8b), the value taken at the plateau only
 523 depends on the subcooling showing three clear limit values.

524

These observations lead to propose a new normalization on the mantle thickness and on the

power escalation period. The mantle thickness is qualitatively related to the thermal boundary layer. In order to account for both turbulent dynamic boundary layer and thermal boundary layer, a relevant approach is to define a normalization quantity as $\delta_T = \delta_\nu / Pr = \alpha / u^*$, with Pr and α being respectively the Prandtl number and the thermal diffusivity of water at the considered inlet conditions. Therefore we define the non-dimensional mantle thickness δ^{++} as

$$\delta^{++} = \frac{\delta}{\delta_T}$$

525 To normalize the power escalation period, we choose to use the time scale linked with the advection
 526 in the mantle, *i.e.* in the streamwise direction, as it corresponds to the major velocity component.
 527 Moreover, as each curve $\delta(\tau)$ converges towards an upper limit (plateau) associated with steady-state
 528 conditions, it seems worth to use this time scale at steady-state in order to assess the transient nature
 529 of the escalation process. Therefore, we define τ_x as

$$\tau_x = \frac{L}{u_{m,\infty}} \quad (22)$$

530 with $u_{m,\infty}$ the value taken by u_m in steady-state. This time scale only depends on the steady-state
 531 quantities and can be obtain analytically. Here "steady-state" is in fact a quasi steady-state and
 532 corresponds to the asymptotic behavior observed for large values of the power escalation period τ .
 533 This is characterized by a quantity, *e.g.* δ in Figure 8 or the CHF value in Figure 5 in [9], which
 534 does not depend on the power escalation period. When τ approaches infinity, Eq.(10) is reduced to
 535 the following equation:

$$\frac{dE_{ss}^*(x^*)}{dx^*} + \frac{v_{m,\infty} L}{u_{m,\infty} \delta_\infty} E_{ss}^*(x^*) = \frac{L}{\delta_\infty} \frac{q_{ss}''}{u_{m,\infty} E_{cr}'''}$$

536 where the subscripts "ss" and " ∞ " stand for steady-state conditions. This differential equation is
 537 solved using the boundary condition $E_{ss}^*(0) = 0$:

$$E_{ss}^*(x^*) = \frac{q_{ss}''}{E_{cr}''' v_{m,\infty}} (1 - e^{-x^*/\lambda}) \quad \text{with} \quad \lambda = \frac{u_{m,\infty} \delta_\infty}{v_{m,\infty} L} \quad (23)$$

538 As $E_{ss}^*(x^*)$ is a increasing function on x^* , the maximum volumetric energy density is observed down-
 539 stream of the heater, *i.e.* $x^* = 1$. Setting $E_{ss}^*(1) = 1$, we obtain the following relation:

$$\frac{1 - e^{-1/\lambda}}{v_{m,\infty}} = \frac{E_{cr}'''}{q_{ss}''} \quad (24)$$

540 Beyond the thermal hydraulics conditions, the left-hand-side term only depends on δ_∞ and the right-
 541 hand-side one only depends on the CHF value at steady-state. The value of τ_x can thus be determined
 542 knowing CHF at steady-state.

543

544 The experimental points are then plotted in Figure 9 using normalized quantities on both axis:

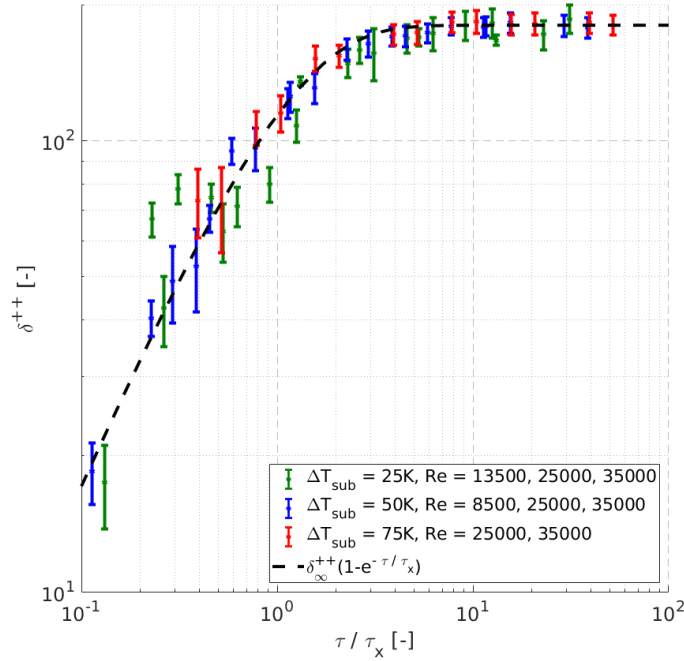


Figure 9: Non-dimensional thickness δ^{++} [-] as a function of the normalized period τ/τ_x [-] for the eight operating conditions ($\Delta T_{sub}, Re$), represented by the error bars. The fitting function (dashed line) corresponds to $\delta_\infty^{++} = 180$.

545 It shows that all available data sets are satisfactorily fitted by the following equation:

$$\delta^{++}(\tau) = \delta_\infty^{++} (1 - e^{-\tau/\tau_x}) \quad (25)$$

546 where δ_∞^{++} is the only tuning parameter and corresponds to the normalized mantle thickness in
 547 steady-state conditions. A single value, equals to 180 in the present case, is suitable for all operating
 548 conditions.

549 4.1.2 Discussion

550 Results presented in Figure 9 show that the quality of the fit between the experimental results and
 551 equation (25) depends on the subcooling. For high subcoolings (50 K and 75 K), the fit is excellent.

552 Indeed, more than 75 % of these points are predicted with ± 5 % error. However, some tests, as-
 553 sociated with short periods ($\tau/\tau_x < 1$) and a small subcooling (25 K) present some discrepancies.
 554 The latter may be explained, supporting the veracity of the our mechanistic assumptions. Indeed, to
 555 be valid, the present model needs a sufficient degree of subcooling so that nucleation-condensation
 556 cycles (NCCs) presented in section 2.2 can take place. However, for a relatively small subcooling
 557 such as 25 K and especially for short periods, the major assumption of the model can reach its limit.
 558 Due to the subcooling, bubbles grow large and have a longer lifetime, about a few milliseconds. It
 559 implies that the duration of a growth and collapse cycle may no longer be negligible in front of the
 560 power escalation period and consequently, the mixing induced by NCCs may be not efficient enough
 561 to make the mantle homogeneous. This explains the excellent fit for all the points, but also the
 562 discrepancies for the points with relatively low subcooling (25 K) and fast transient ($\tau/\tau_x < 1$).
 563

564 Equation (25) proposes a simple relation between the mantle thickness δ through its non-dimensional
 565 form δ^{++} and the different working parameters. This shows that the model is able to accurately
 566 handle the different working parameters. Equation (25) includes a unique non *a priori* calculable
 567 constant δ_{∞}^{++} which corresponds to the value taken by the normalized mantle thickness at steady-
 568 state for all the conditions of this set. The fit with the experimental data gives δ_{∞}^{++} equals 180 for
 569 the current set of conditions. However, this quantity is expected to depend on other parameters such
 570 as the pressure or the quantity λ defined in Equation (23). The quantity λ represents the ratio at
 571 steady-state between heat removal in the x and the y directions. It linearly depends on the heated
 572 length L . For the current set of experimental conditions, λ takes values close to unity or above,
 573 meaning that heat removal in the x direction prevails or is equivalent to that in the y direction. If
 574 considering cases where the heat removal in the y direction significantly prevails, one would expect
 575 the constant δ_{∞}^{++} to decrease since in this case heat transfer involves the whole length of the heater.
 576

577 The present model relies on an energy balance in the fluid and does not take into account the
 578 surface condition of the heater. Nonetheless, it is known that boiling phenomena, including boiling
 579 crisis, depend on key parameters which are surface conditions: nucleation site density, roughness,
 580 wettability, porosity. In our experiments, the exponential electrical heat input is released either in
 581 the substrate or to the water. The proportion in time of each part is determined by the effusivity of
 582 both media (water and sapphire) and by the surface conditions once the boiling occurs. Therefore,
 583 our approach implicitly takes into account the surface conditions as well as the thermal inertia of the

584 substrate via the time function $q_w''(t)$, defined as the net heat flux released to the water. Moreover, at
585 such a high degree of subcooling, bubbles present a high-frequency pulsating behavior which establish
586 NCCs, mixing the fluid in the mantle. It is then reasonable to assume that the major phenomenon
587 leading to boiling crisis is the transient heating process in the mantle as described in equation (9).
588 This would certainly not be the case for lower subcooling.

589
590 Mechanistically speaking, the usability range of the model is related to the occurrence of the
591 assumed mechanisms: *i.e.* the homogenization of the mantle temperature throughout the action of
592 the NCCs and the cooling processes characterized by the velocities u_m and v_m .
593 For instance, in case of pool boiling, the velocity v_m , based on turbulent velocity fluctuations, is not
594 even defined. Moreover, in such a case, the definition and the existence of a homogeneous mantle is
595 questionable as the physical mechanism governing the wall-vicinity cooling is significantly different.
596 Besides, in case of really short transients ($\tau < 5 \text{ ms}$), all nucleation sites may be activated simulta-
597 neously on the wall. Therefore, as observed by Kossolapov et al. [9], the boiling crisis can directly
598 be triggered at ONB by coalescence of the first generation of bubbles. Furthermore, even if some
599 generations of bubbles occur, the time spent in nucleate boiling regime may be too short to let the
600 NCCs sufficiently homogenize the mantle. Moreover, the lifespan of a bubble (about 0.05 ms) may
601 become non-negligible compared to the power escalation period if the latter becomes too small, going
602 against one of the modeling assumptions.

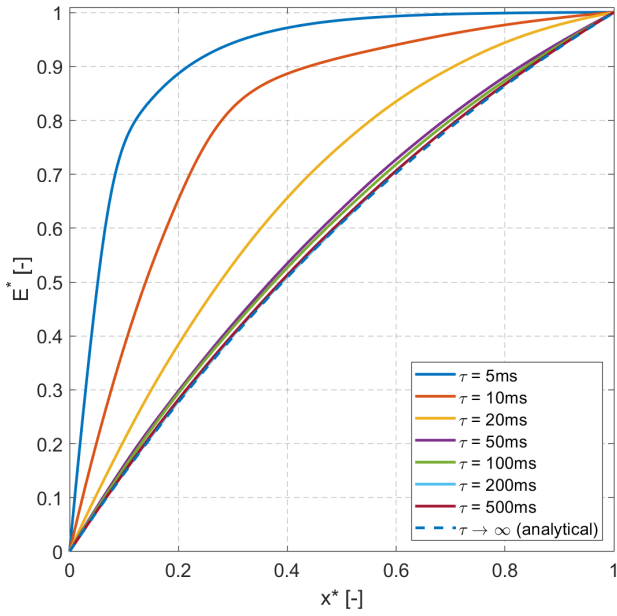
603 Conversely, at a pressure higher than the atmospheric one, the model might still be usable. Indeed,
604 a slight increase of the pressure would decrease the bubble size and thus the mantle thickness, NCCs
605 should still occur and homogenize the mantle. However, if the pressure rises too much beyond the
606 atmospheric pressure, *i.e.* beyond a few tens of bars, bubbles might be too small to let the NCCs to
607 happen. Indeed, bubbles may for example not grow enough to go beyond the superheated layer, and
608 thus cannot re-condense.

609
610 Finally, some computation assumptions must be discussed. In a first hand, as presented in
611 section 3.3, v_m is computed using single-phase DNS data of turbulent velocity fluctuations whereas
612 the latter is most likely increased by the bubble growth and collapse. However, the quantification
613 of this increase is currently out of range. In a second hand, the same equation is used during the
614 entire transient whereas during the single-phase regime, there is no NCC and thus the mantle does
615 not have a physical meaning. During this regime, the energy is not homogenized as there is no

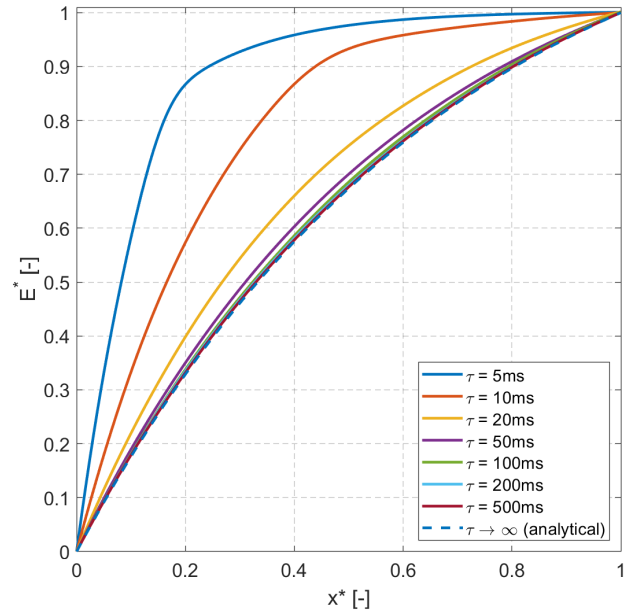
616 NCC and is mostly confined in the conductive thermal boundary layer. For a given condition, this
 617 conductive boundary layer is much smaller than the associated mantle thickness. For instance, at 75
 618 K of subcooling and a period of 5 ms, the conductive layer is about 30 μm thick ($\sim \sqrt{\alpha \tau}$) whereas
 619 the mantle is 100 μm thick (see Figure 8a). Consequently, the energy released in the liquid is more
 620 restrained close to the wall where the flow is not as efficient too dissipate the energy. Therefore,
 621 during the single-phase regime, the model in fact uses dissipation processes more efficient than it
 622 should be. Nonetheless, this discrepancy is strongly attenuated as during the single-phase regime,
 623 the energy released in the liquid is low and so the energy in the mantle, implying that the energy
 624 dissipated by the model is also low (being a function of E'''). In order to ensure that this dissipation
 625 discrepancy is low, we realized a sensibility test where during the single-phase regime, no dissipation
 626 is computed and all the energy remains in the mantle in order to consider the limit case. The
 627 calculation shows that the mantle thickness almost does not vary, the discrepancy being only a few
 628 percents, supporting the fact that using the dissipation terms of the model during the entire transient
 629 does not significantly impact the results.

630 4.2 Energy distribution along the heated wall

631 Solving the energy balance (Equation (10)) allows one to access the function $E^*(x^*, t^*)$. The volu-
 632 metric energy density rise is plotted in Figure 10 as a function of the distance x^* , at time $t^* = t_{CHF}^*$
 633 corresponding to the time of boiling crisis. Results are presented for two conditions of subcooling,
 634 50 K (Figure 10a) and 75 K (Figure 10b). Both cases include seven values of the time-period τ and
 635 the analytic solution for steady-state condition (Equation (23)).



(a) $\Delta T_{sub} = 50 K$



(b) $\Delta T_{sub} = 75 K$

Figure 10: $E^*(x^*, t_{ch,f}^*) [-]$ for 50 K and 75 K of subcooling, for Reynolds number of 35000 and a time-period ranging within 5 ms to 500 ms. The analytic solution corresponds to the steady-state case, given by Equation (23).

636 Figure 10 shows that the set of curves is very similar at 50 K and 75 K. This result confirms
637 the relevance of the dimensionless approach. The volumetric energy density rise is seen to increase
638 with the coordinate x^* . As expected, boiling crisis is more likely to happen downstream the heated
639 plate for long time-periods, greater than 20 ms, as a regular increase of E^* with x^* is noticeable in
640 both Figures. About 20 percent of the plate length ($0.8 < x^* < 1$) is associated with a volumetric
641 energy density in the mantle greater than 90% of the critical energy. One will also note that curves
642 with a time period longer than 50 ms almost overlap, nearly matching the analytic solution derived
643 for an infinite time-period. A different behavior should be observed for very fast transients. The
644 curves presented in Figure 10 for the shortest time-periods, *i.e.* 5 ms and 10 ms, reveal a different
645 increase of the volumetric energy density rise with x^* . For $\tau = 10$ ms, more than 50 percent of the
646 plate length ($0.5 < x^* < 1$) has a volumetric energy density in the mantle greater than 90% of the
647 critical energy. This ratio increases up to 80% for $\tau = 5$ ms. One expects therefore a large dry
648 spot to occur and to cover most of the plate. The existence of these two regimes of boiling crisis is
649 confirmed experimentally. A link with the two non dimensional groups N_x and N_y will be shown in
650 the following section.

651 4.3 Impact of the non dimensional groups N_x and N_y on boiling crisis

652 The energy balance equation (10) includes two non dimensional groups defined as:

$$N_x = \frac{u_m \tau}{L} \quad N_y = \frac{v_m \tau}{\delta}$$

653 These quantities are intrinsically connected with the mantle thickness δ as they involve the charac-
 654 teristic velocities u_m and v_m . The iterative solving procedure of Equation (9) yields a single couple
 655 (N_x, N_y) for each experimental run. These quantities are plotted as a function of the time period τ
 656 in Figure 11.

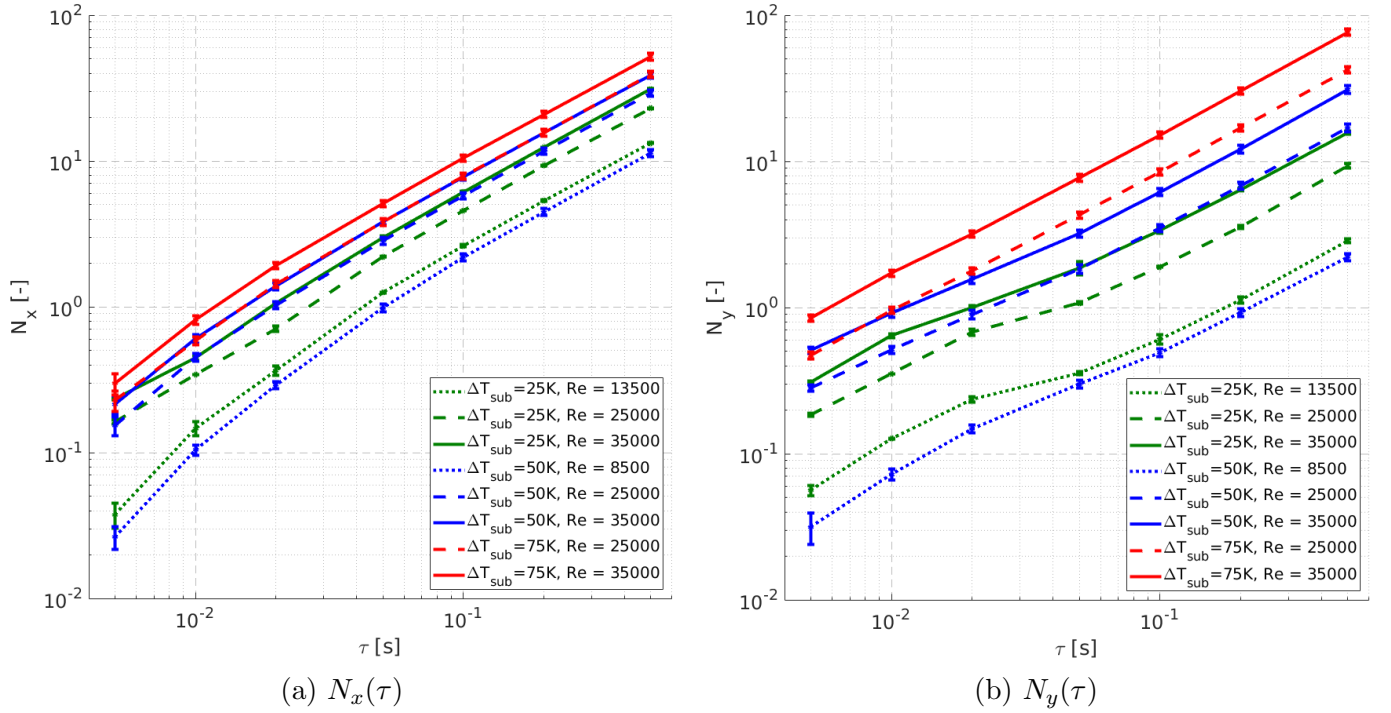


Figure 11: Dimensionless groups N_x and N_y [-] versus the excursion period τ [s]

657 4.3.1 Physical meaning of N_x

658 The group N_x is the ratio of two characteristic times: τ which is the power excursion period, and
 659 L/u_m which is the time needed for a fluid particle to travel in the mantle from the inlet ($x = 0$ *i.e.*
 660 $x^* = 0$) to the outlet section ($x = L$ *i.e.* $x^* = 1$).

661 Value of N_x smaller than unity means that the fluid particle is "trapped" in the heated mantle
 662 during the period τ . As a result, the temperature of the mantle increases. In contrast, N_x greater
 663 than unity means that the fluid particle has enough time to be advected alongside the heated area
 664 during a time period τ . The temperature of the mantle is slightly modified. From the mathematical
 665 point of view, the group N_x represents the magnitude of the spatial variations in the flow direction.

666 No energy gradient should be observed in the limit of a zero value leading to a homogeneous incip-
667 ience of boiling crisis all over the heated plate: the flow is "frozen". On the opposite, large values
668 of N_x correspond to a strong variation in the vertical direction; boiling crisis is expected to happen
669 in the form of dry spots localized downstream the plate. These two predicted regimes are confirmed
670 by experiments as presented in Figure 12. In terms of heat removal, N_x can also be interpreted as
671 the efficiency of the system to release the input of energy from the heater in the streamwise direction.

672

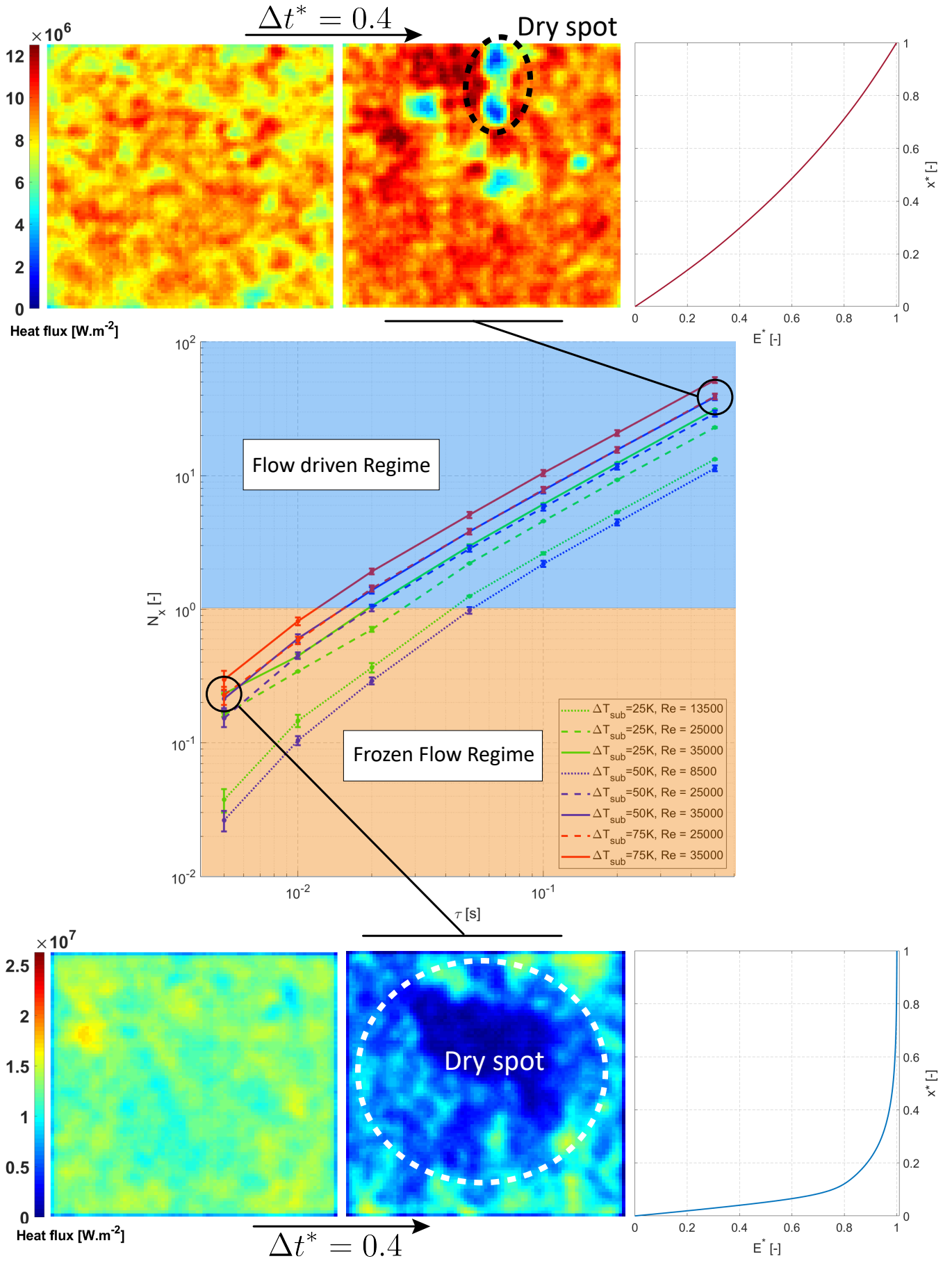


Figure 12: Boiling and energy patterns for different values of N_x . The maps represent the heat flux pattern at the boiling crisis (right maps) and 0.4τ prior the boiling crisis (left maps). The right right curves represent the energy density distribution $E^*(x^*)$ at the boiling crisis. The water flows upwards and the conditions are $\Delta T_{sub} = 50 \text{ K}$, $Re = 35000$ and $p = 1 \text{ bar}$.

673 For the experiments presented by Kossolapov et al. in [9], the heating cell is 1 cm in length.
674 For conditions of $Re = 35000$ and $\Delta T_{sub} = 75 K$, the frozen flow regime is observed for a time
675 period $\tau \leq 10ms$ while the flow driven regime happens for $\tau \geq 20ms$. One expects these values to
676 be modified by a change in the heater length. Other experiments have been conducted using the
677 same channel and similar thermohydraulic conditions but with a longer heater, 4 cm in length. The
678 quantity N_x becomes equal to 0.73 when the power excursion period $\tau = 50$ ms, now corresponding to
679 the frozen flow regime. The space-variation of the volumetric energy density rise at $t=t_{CHF}$ and the
680 heat flux field measured on the heated plate obtained for these conditions are presented in Figure 13.
681 The energy profile shows a plateau for x^* greater than 0.4. The heat flux distribution clearly reveals
682 two distinct areas. At the inlet part of the plate ($x^* \leq 0.4$) a large amount of heat flux is released
683 in the fluid while beyond $x^* = 0.4$, many spots of small heat flux are visible revealing that dry spots
684 are present in this area.

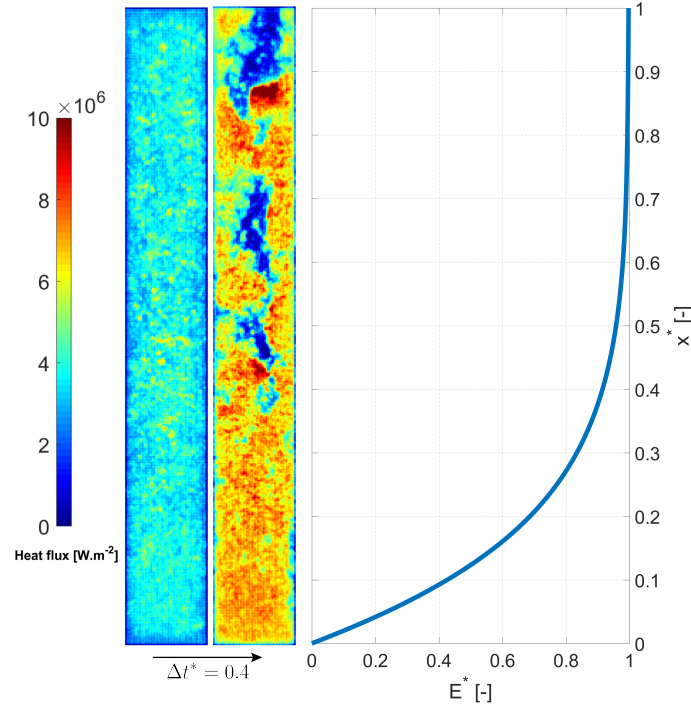


Figure 13: Boiling and energy patterns for a $4 \times 0.6 \text{ cm}^2$ heating cell. The maps represent the heat flux pattern at the boiling crisis (right map) and 0.4τ prior the boiling crisis (left map). The right curve represents the energy density distribution $E^*(x^*)$ at the boiling crisis. The water flows upwards and the conditions are $\Delta T_{sub} = 50 K$, $Re = 35000$ and $p = 1 \text{ bar}$, $\tau = 50 \text{ ms}$ ($N_x = 0.73$).

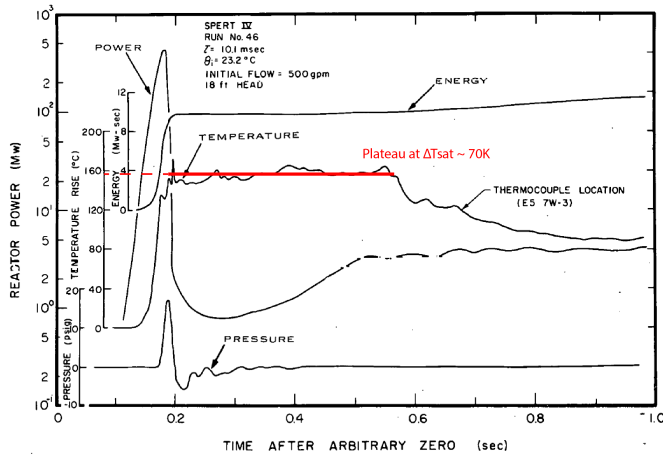
685 From the previous analysis, N_x appears to be a relevant quantity, more than the period τ ,
686 to predict the location for boiling crisis to occur, i.e. homogeneously along the heater or localized
687 downstream the heater. Indeed, considering the same time period as in Figure 13, i.e. $\tau = 50 \text{ ms}$ but
688 the 1 cm-long heater, boiling crisis occurs, localized only at the downstream extremity of the heater.
689 This feature is not surprising as these experimental conditions correspond to $N_x = 5$. This conclusion

690 may be useful for industrial applications, particularly for nuclear industry. If considering for instance,
 691 an accidental scenario of the BORAX-type, the computation of N_x would give information on the
 692 particular zones where the fuel rods could be damaged. If the thermohydraulic conditions and the
 693 power escalation period correspond to a high value of the N_x group, reaching the boiling crisis would
 694 only damage the downstream part of the core, whereas a small value of N_x would imply the possible
 695 failure of the entire core.

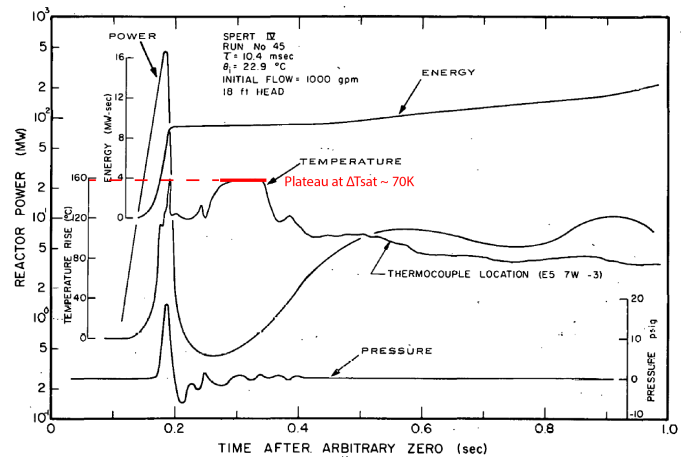
696 4.3.2 Interpretation of N_y and experimental evidences

697 The non-dimensional group N_y represents the ratio between two characteristic times, τ the power
 698 excursion period, and δ/v_m which is the time needed for a fluid particle, located at the boundary
 699 bulk-mantle, to travel away from the wall over a length δ at the velocity v_m . Qualitatively, N_y is the
 700 number characterizing the efficiency of the system to transfer energy from the mantle to the bulk in
 701 the direction normal to the wall via the turbulent fluctuations of the normal velocity. N_y increases
 702 with the Reynolds number.

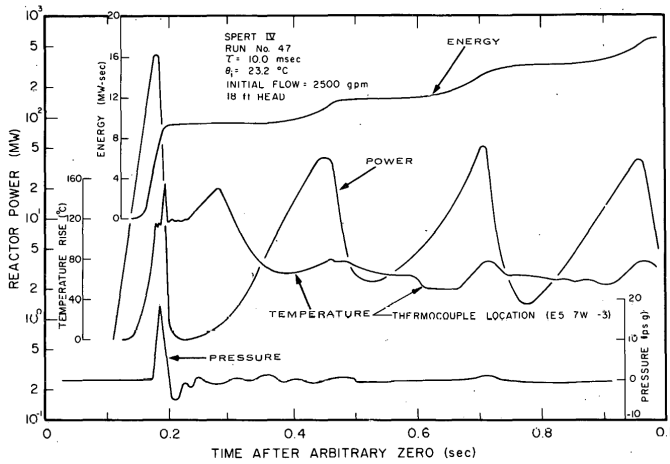
703
 704 The role of this group N_y can be illustrated considering the results obtained in 1964 with the
 705 SPERT IV facility [4]. A power pulse was applied in 64 cm tall fuel plates. The fluid was highly
 706 subcooled ($\Delta T_{sub} \sim 90$ K) flowing between the fuel plates with a bulk velocity up to $U_{bulk} = 3.7$ m.s⁻¹.
 707 As the characteristic velocity u_m is much smaller than U_{bulk} , N_x can be highly maximized by $U_{bulk}\tau/L$.
 708 All runs conducted with a power escalation period equal to 10 ms, lead to N_x values smaller than 0.1
 709 due to the large value of L . This situation corresponds to the "frozen regime". Various tests reported
 710 in [4] are presented in Figure 14. All recordings were performed with a similar power input and a
 711 time-period τ of ten milliseconds. The only change in the tests was the bulk velocity as indicated in
 712 Figure 14. At low velocity (Tests B-23 and B-29), a temperature plateau is observed, 70 K above the
 713 saturation temperature. This does not happen for the highest velocities (Tests B-33 and B-39) where
 714 smaller temperature excursions are observed. With the increase of the flow rate, a better cooling
 715 is achieved as the bulk velocity and the turbulent fluctuations increase. Since N_x is small for these
 716 four configurations ($N_x < 0.1$), the streamwise cooling process is always weak and thus cannot be
 717 the discriminating phenomenon explaining the different observations. Conversely, with the increase
 718 of the flow rate and so of the turbulence, the velocity v_m increases and so N_y and the cooling process
 719 normal to wall, preventing the occurrence of boiling crisis for the test B-33 and B-39.



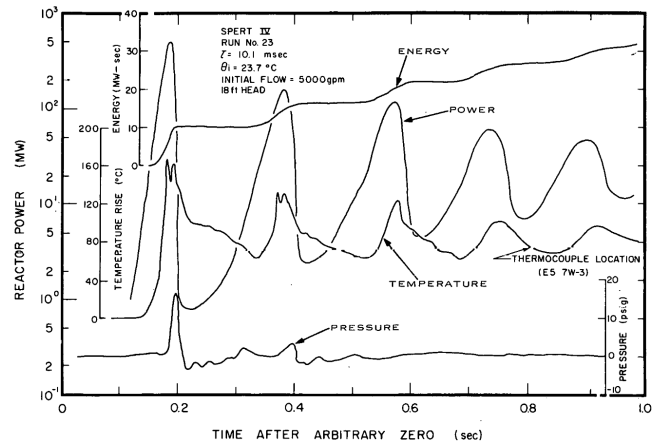
(a) Test B-23 — $0.4m.s^{-1}$



(b) Test B-29 — $0.7m.s^{-1}$



(c) Test B-33 — $1.8m.s^{-1}$



(d) Test B-39 — $3.7m.s^{-1}$

Figure 14: SPERT IV test results for 10 ms power excursion period with different flow conditions (adapted from [4]).

720 Lastly, the flow conditions to be considered for the prediction of boiling crisis deserve a few com-
 721 ments. Quantities usually mentioned in the literature are either the bulk velocity U_{bulk} [$m.s^{-1}$], the
 722 mass flux G [$kg.m^{-2}.s^{-1}$] or the Reynolds number Re [-]. Nevertheless, these quantities are relevant
 723 if considering the flow in the whole cross-section. As discussed in the present work, for high sub-
 724 cooling and strong forced convection, physical phenomena involved in the occurrence of boiling crisis
 725 are located in the region near the wall, whose characteristic length scale is the mantle thickness δ .
 726 Therefore the relevant quantities to be used for these specific conditions should be the wall quantities,
 727 namely the wall Reynolds number Re_{τ} [-], the shear velocity u^* [$m.s^{-1}$] and the viscous sub-layer
 728 unit δ_{ν} [m].

729

730 5 Conclusions and Perspectives

731 We have presented a new model aiming to describe the flow boiling crisis generated by exponential
732 power transients at high subcooling and atmospheric pressure. The model is based on the novel
733 experimental insight offered by the work of by Kossolapov et al. who used synchronized high speed
734 video and IR thermometry with high resolution diagnostics [9]. Particularly, this model accounts
735 for the mechanism of nucleation and condensation cycles (NCCs) not previously taken into account
736 to model boiling crisis for such conditions of high subcooling. The model includes heat removal
737 contributions in both streamwise and normal directions using turbulent flow characteristics.

738
739 The present model makes use of a physical *a priori* unknown quantity which is the mantle
740 thickness δ . Using a non-dimensional approach, we have shown that this quantity verifies a simple
741 mathematical relation involving the operating conditions and a unique experimental tuning constant
742 δ_{∞}^{++} common to all investigated tests. The fit between the experimental points and the latter relation
743 is excellent for highly subcooling conditions, *i.e.* for 50 K of subcooling and more, which are the
744 most relevant for nuclear safety applications. The fitting is also excellent at 25 K of subcooling for
745 long periods, *i.e.* for $\tau/\tau_x > 1$, which reveals the validity limit in term of subcooling of our approach.
746 The quality of this fitting shows that from this simple formulation, the model is able to take into
747 consideration the different operating parameters explaining the role of each. Moreover, the two non-
748 dimensional groups N_x and N_y arising in the model provide physical explanations for experimental
749 observations. The group N_x appears as a predicting tool to explain spatial occurrence of the boiling
750 crisis on the heating wall, *i.e.* homogeneously along or localized downstream the heater. This result
751 can be usefully applied for instance in nuclear safety as it allows to predict the localization of the
752 failed fuel during an accident. The group N_y , quantifies the contribution of heat removal in the
753 transverse direction due to turbulent velocity fluctuations. It brings into light effects observed in
754 large-scale reactor tests.

755
756 The present work investigates exponential power transients and homogeneous heat flux fields. An
757 extension to other types of transients and to heterogeneous heat flux fields is however possible as
758 the current mathematical formulation of the model allows it. Finally, a better understanding of the
759 constant δ_{∞}^{++} would enable the present model to become fully predictive. The impact of the pressure
760 and on the parameter λ are currently in progress.

761 Acknowledgment

762 This work has been supported by the French Alternative Energies and Atomic Energy Commission
763 through the CEA contract number 4000800674/P5B62 and MIT contract number 6938370.

764 References

- 765 [1] Y. Wu, Neutronics of Advanced Nuclear Systems. Springer, 2019.
- 766 [2] J. R. Dietrich and D. C. Layman, “Transient and steady state characteristics of a boiling reactor.
767 the borax experiment, 1953,” 2 1954.
- 768 [3] R. W. Miller, A. Sola, and R. K. McCardell, “Report of the Spert I Destructive Test Program
769 on an Aluminum , Reactor,” Ido-16883, 6 1964.
- 770 [4] J. G. Crocker and L. A. Stephan, “Reactor Power Excursion Tests in the SPERT IV Facility,”
771 Ido-17000, 8 1964.
- 772 [5] M. Ishikawa and T. Inabe, The Nuclear Safety Research Reactor (NSRR) in Japan, pp. 285–334.
773 Boston, MA: Springer US, 1979.
- 774 [6] J. Papin, M. Balourdet, F. Lemoine, F. Lamare, J. M. Frizonnet, and F. Schmitz, “French
775 studies on high-burnup fuel transient behavior under ria transient,” Nuclear Safety, 10 1996.
- 776 [7] H. A. Johnson, “Transient boiling heat transfer to water,” International Journal of Heat and
777 Mass Transfer, vol. 14, no. 1, pp. 67–82, 1971.
- 778 [8] I. Kataoka, A. Serizawa, and A. Sakurai, “Transient boiling heat transfer under forced convec-
779 tion,” International Journal of Heat and Mass Transfer, vol. 26, no. 4, pp. 583 – 595, 1983.
- 780 [9] A. Kossolapov, F. Chavagnat, R. Nop, N. Dorville, B. Phillips, J. Buongiorno, and M. Bucci,
781 “The boiling crisis of water under exponentially escalating heat inputs in subcooled flow boiling
782 at atmospheric pressure,” International Journal of Heat and Mass Transfer, 2020.
- 783 [10] G. P. Celata, M. Cumo, and A. Mariani, “Assessment of correlations and models for the predic-
784 tion of CHF in water subcooled flow boiling,” vol. 37, no. 2, pp. 237–255, 1994.
- 785 [11] G. P. Celata and A. Mariani, Critical Heat Flux, Post-CHF Heat Transfer and Their
786 Augmentation, pp. 325–382. Vienna: Springer Vienna, 2003.

- 787 [12] S. G. Kandlikar, “Critical heat flux in subcooled flow boiling - An assessment of current un-
788 derstanding and future directions for research,” Multiphase Science and Technology, vol. 13,
789 no. 3-4, p. 26, 2001.
- 790 [13] H. Zhang, I. Mudawar, and M. M. Hasan, “Investigation of interfacial behavior during the
791 flow boiling CHF transient,” International Journal of Heat and Mass Transfer, vol. 47, no. 6-7,
792 pp. 1275–1288, 2004.
- 793 [14] W. H. Ahmed, M. A. El-Nakla, and B. I. Ismail, “Towards understanding the critical heat flux for
794 industrial applications,” International Journal of Multiphase Flow, vol. 36, no. 3, pp. 153–165,
795 2010.
- 796 [15] Y. Haramura and Y. Katto, “A new hydrodynamic model of critical heat flux, applicable
797 widely to both pool and forced convection boiling on submerged bodies in saturated liquids,”
798 International Journal of Heat and Mass Transfer, vol. 26, no. 3, pp. 389–399, 1983.
- 799 [16] C. Lee and I. Mudawar, “A mechanistic critical heat flux model for subcooled flow boiling based
800 on local bulk flow conditions,” International Journal of Multiphase Flow, vol. 14, no. 6, pp. 711
801 – 728, 1988.
- 802 [17] Y. Katto, “A prediction model of subcooled water flow boiling CHF for pressure in the range
803 0.1-20 MPa,” International Journal of Heat and Mass Transfer, vol. 35, no. 5, pp. 1115 – 1123,
804 1992.
- 805 [18] G. Celata, M. Cumo, A. Mariani, M. Simoncini, and G. Zummo, “Rationalization of exist-
806 ing mechanistic models for the prediction of water subcooled flow boiling critical heat flux,”
807 International Journal of Heat and Mass Transfer, vol. 37, pp. 347 – 360, 1994.
- 808 [19] A. Serizawa, “Theoretical Prediction of Maximum Heat Flux in Power Transients,” International
809 Journal of Heat and Mass Transfer, vol. 26, no. 6, pp. 921–932, 1983.
- 810 [20] K. Pasamehmetoglu, R. Nelson, and F. Gunnerson, “Critical heat flux modeling in pool boiling
811 for steady-state and power transients,” Journal of Heat Transfer (Transactions of the ASME,
812 Series C); (United States), vol. 112:4, 11 1990.
- 813 [21] A. Richenderfer, A. Kossolapov, J. H. Seong, G. Saccone, E. Demarly, R. Kommajosyula,
814 E. Baglietto, J. Buongiorno, and M. Bucci, “Investigation of subcooled flow boiling and chf

- 815 using high-resolution diagnostics,” Experimental Thermal and Fluid Science, vol. 99, pp. 35 –
816 58, 2018.
- 817 [22] M. Bucci, A. Richenderfer, G.-Y. Su, T. McKrell, and J. Buongiorno, “A mechanistic ir cali-
818 bration technique for boiling heat transfer investigations,” International Journal of Multiphase
819 Flow, vol. 83, pp. 115 – 127, 2016.
- 820 [23] F. Chavagnat, R. Nop, N. Dorville, B. Phillips, and M. Bucci, “Single-phase heat transfer
821 regimes in forced flow conditions under exponential heat inputs,” International Journal of Heat
822 and Mass Transfer, vol. 174, p. 121294, 2021.
- 823 [24] M. W. Rosenthal, “An experimental study of transient boiling,” Nuclear Science and
824 Engineering, vol. 2, no. 5, pp. 640–656, 1957.
- 825 [25] A. Sakurai and M. Shiotsu, “Transient Pool Boiling Heat Transfer—Part 1: Incipient Boiling
826 Superheat,” Journal of Heat Transfer, vol. 99, pp. 547–553, 11 1977.
- 827 [26] A. Sakurai and M. Shiotsu, “Transient Pool Boiling Heat Transfer—Part 2: Boiling Heat Trans-
828 fer and Burnout,” Journal of Heat Transfer, vol. 99, pp. 554–560, 11 1977.
- 829 [27] G.-Y. Su, M. Bucci, T. McKrell, and J. Buongiorno, “Transient boiling of water under expo-
830 nentially escalating heat inputs. Part I: Pool boiling,” International Journal of Heat and Mass
831 Transfer, vol. 96, pp. 667 – 684, 2016.
- 832 [28] G.-Y. Su, M. Bucci, T. McKrell, and J. Buongiorno, “Transient boiling of water under expo-
833 nentially escalating heat inputs. Part II: Flow boiling,” International Journal of Heat and Mass
834 Transfer, vol. 96, pp. 685 – 698, 2016.
- 835 [29] J. Weisman and B. S. Pei, “Theoretical prediction of maximum heat flux in power transients,”
836 International Journal of Heat and Mass Transfer, vol. 26, no. 10, pp. 1463–1477, 1983.
- 837 [30] L. Tong, H. Currin, P. Larsen, and O. Smith, “Influence of axially non-uniform heat flux on
838 dnb,” Chem. Eng. Progr., Symp. Ser., 62: No. 64, 35-40(1966)., 1 1966.
- 839 [31] N. E. Todreas and M. S. Kazimi, Nuclear Systems I: Thermal Hydraulic Fundamentals. New
840 York: Hemisphere Publishing Co., 1990.
- 841 [32] J. Graham, K. Kanov, X. I. A. Yang, M. Lee, N. Malaya, C. C. Lalescu, R. Burns, G. Eyink,
842 A. Szalay, R. D. Moser, and C. Meneveau, “A web services accessible database of turbulent

843 channel flow and its use for testing a new integral wall model for les,” Journal of Turbulence,
844 vol. 17, no. 2, pp. 181–215, 2016.

845 [33] R. D. Moser, J. Kim, and N. N. Mansour, “Direct numerical simulation of turbulent channel
846 flow up to $Re_\tau = 590$,” Physics of Fluids, vol. 11, no. 4, pp. 943–945, 1999.

847 **A Appendix - DNS analysis**

848 **A.1 Computation method of the determination of the velocity v_m**

849 DNS simulations performed by Moser et al. [33] investigated turbulent flows inside a rectangular
850 channel. Their data yield Probability Density Functions (PDF) as a function of the distance to the
851 wall and for three values of the Re_τ parameter (180, 395 and 590). Graham et al. [32] performed
852 similar DNS simulations with $Re_\tau = 1000$ and made available instantaneous velocity fields in steady-
853 state conditions.

854
855 For Re_τ equals 180, 395 and 590, Moser et al. propose in their data sets, the PDFs of v' for
856 different y^+ from the wall to the channel centerline. The use of equation (19) at each available y^+
857 enables then to compute the expected value v_m^+ for the three values of Re_τ (see figure 16a).

858
859 For Re_τ equals 1000, Graham et al. propose in their database the full velocity field of their
860 simulation. The simulation domain consists of a mesh made of $2048 \times 512 \times 1436$ nodes and the
861 database presents 4000 snapshots of the field. In the x and z directions, the domain is periodic. The
862 authors provide statistic quantities of the flow such as the mean velocities or the Root Mean Square
863 (RMS) compounds, but not the actual PDF needed to calculate v_m . It is then necessary to first
864 compute the expected value v_m from the raw statistics. In order to have enough points to compute
865 the expected value, we assume the ergodic hypothesis: for a given y coordinate, a quantity X verifies
866 $\bar{X} = \langle X \rangle_{x,z}$, which are respectively the temporal average for a given position and the space average
867 in a plan $x - z$ for a given time. By symmetry, we will only investigate half of the channel in the
868 y direction, *i.e.* between the wall and the channel centerline. A node over two will be taken into
869 account in this direction as this reduction gives a satisfactorily fine information on the field v_m and
870 reduces the computation time. For each y coordinate analyzed, all the $x - z$ nodes of the y -constant
871 layer are used to compute the expected value. We also combine the data of three randomly chosen

872 time steps in order to smooth a potential punctual statistic event, such as vortices. Then, each value
 873 v_m is obtained from a statistic made of $2048 \times 1536 \times 3$ points, *i.e.* more than nine millions points.
 874 The following procedure aims to validate the fact that this sample size is satisfactorily large.

875

876 To investigate the statistical convergence, let us define two quantities: the normalized mean trans-
 877 verse velocity V^+ and the two v_m^+ components computed with the positive and negative fluctuations.
 878 From a finite statistic sample of N observations of normalized transverse velocities v_n^+ , V^+ is defined
 879 as

$$V^+ = \mathbb{E}(v' | \mathbb{R}) = \sum_{n=1}^N \frac{v_n^+}{N} \quad (26)$$

880 This quantity theoretically equals zero. We also define two v_m^+ components

$$v_{m,v'>0}^+ = \mathbb{E}(v' | \mathbb{R}^+) = \frac{1}{N} \sum_{v_n^+>0} v_n^+ \quad v_{m,v'<0}^+ = \mathbb{E}(v' | \mathbb{R}^-) = -\frac{1}{N} \sum_{v_n^+<0} v_n^+ \quad (27)$$

881 where $v_{m,v'>0}^+$ is v_m^+ computed with the positive fluctuations and $v_{m,v'<0}^+$ is v_m^+ computed with the
 882 negative fluctuations. These values theoretically compensate each other. In figure 15, we present the
 883 value taken by these three quantities as a function of the sample size N .

884

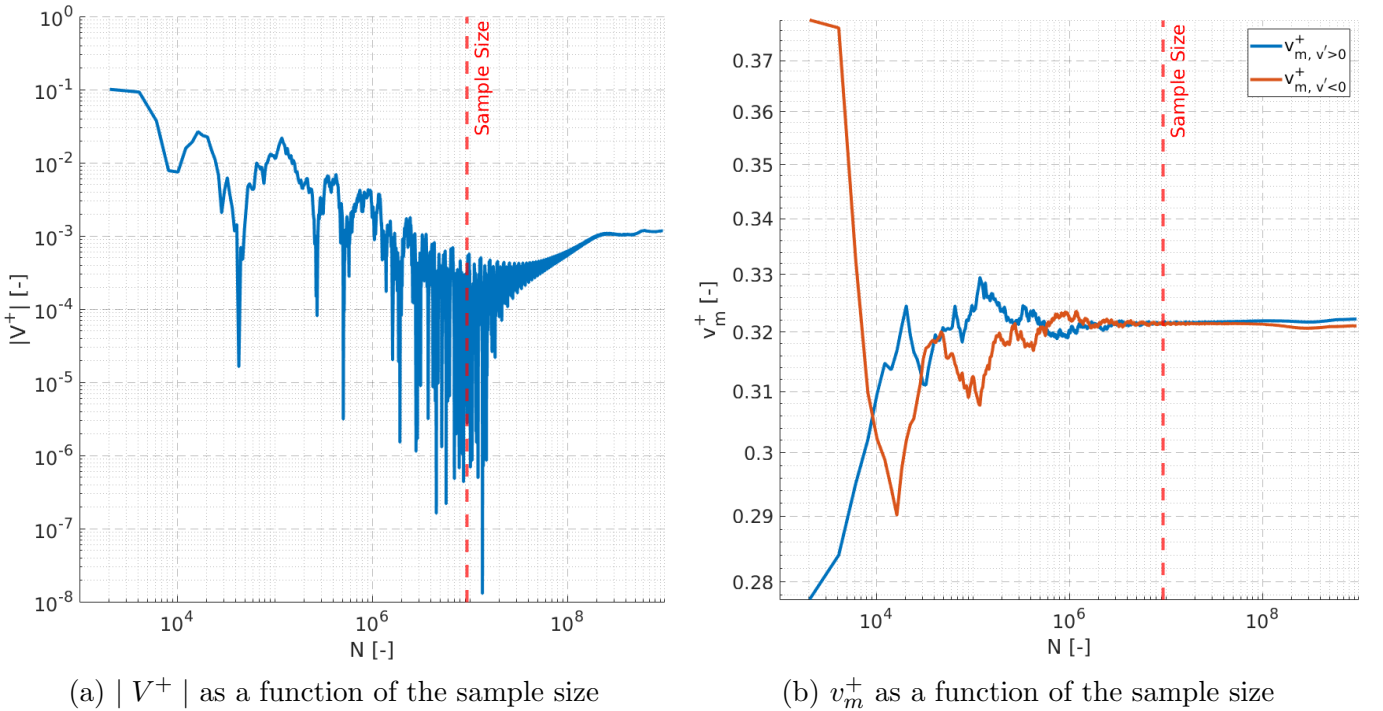


Figure 15: Statistic convergence analysis for the set $Re_\tau = 1000$ of Graham et al. [32] and $y^+ = 41$. The quantities are plotted as functions of the sample size N . The dashed line corresponds to the sample size taken for the upcoming computation, *i.e.* $2048 \times 1536 \times 3$.

885 Qualitatively, $v_{m,v'>0}^+$ and $v_{m,v'<0}^+$ fluctuate for small values of N and converge to a common value
 886 for larger values. Particularly, they have converged for the sample size $2048 \times 1536 \times 3$ (see figure
 887 15b) which is represented by the vertical dashed line. More quantitative criteria can be assessed
 888 with the mean velocity. First of all, for the sample size $2048 \times 1536 \times 3$, the absolute value taken by
 889 the mean velocity is negligible compared to the characteristic velocity of the channel flow, *i.e.* the
 890 shear velocity u^* : $|V^+| = |V|/u^* < 10^{-3}$ (see figure 15a). Moreover, the mean velocity is negligible
 891 compared to our quantity of interest, v_m , which is the most relevant criterion for our computations:

$$\frac{|V^+|}{v_m^+} < 10^{-2} \quad (28)$$

892 This confirms that for a sample size of $2048 \times 1536 \times 3$ observations, V^+ has converged to zero. Thus
 893 this sample size is adequate for the calculation of v_m^+ . Lastly, we will take v_m^+ as the average of the
 894 two definitions, $v_m^+ = \frac{1}{2}(v_{m,v'>0}^+ + v_{m,v'<0}^+)$.

895 A.2 Comparative study on the methods to compute v_m

896 After having defined the method to compute the expected value v_m , let us compare our results with
 897 the ones of Weisman and Pei, and of Pasamehmetoglu which need less computing resources. The
 898 formulation of their characteristic velocity is:

$$\mathbb{E}(v' - v_v | [v_v, +\infty]) = \int_{v_v}^{+\infty} (v' - v_v)P(v') dv' \quad (29)$$

899 where the PDF $P(v')$ is defined with an assumed analytic expression and v_v the vapor ejection
 900 velocity, which is taken null in our case as explained in section 3.3. Pasamehmetoglu assumed a
 901 hyperbolic distribution, $P(v') \propto (1/v')^n$ with n , an adjustable empirical coefficient taken in the
 902 interval $]2, +\infty[$. In order to fit his model with the experimental data set, n is taken equal to 4. In
 903 our case, v_v is taken null and the computation of the expected value Eq. (29) corresponds to the
 904 integral $\int_0^{+\infty} dx/x^{n-1}$, which diverges. Consequently, the approach of Pasamehmetoglu cannot be
 905 used in our case. In their approach, Weisman and Pei assumed that $P(v')$ has a Gaussian distribution
 906 everywhere in the domain, *i.e.* $\forall y^+ \in [0, Re_\tau]$:

$$P_{wp}(v') = \frac{e^{-\frac{1}{2}\left(\frac{v'}{v_{rms}}\right)^2}}{v_{rms}\sqrt{2\pi}} \quad (30)$$

907 This assumption is relevant in the bulk, but is not true near the wall where anisotropy effects deviate
 908 the probability density function from a Gaussian distribution. In order to quantify the discrepancy
 909 between this assumption and the actual fluctuations extracted from the DNS data, we compare the
 910 expected values $v_m = \mathbb{E}(v' | \mathbb{R}^+)$ computed with the Gaussian distribution ($v_{m,wp}^+$) with the ones
 911 computed with DNS data as above (v_m^+). The relative discrepancy is defined as

$$\frac{|v_m^+ - v_{m,wp}^+|}{v_m^+} \quad (31)$$

912 The comparison is plotted in Fig. 16b. A maximum difference of about 50 %, is observed at $y^+ = 5$
 913 and reduces as the distance increases, being about 5 % at $y^+ = 50$. As the present study concerns
 914 near wall phenomena, we decided to use DNS data to compute v_m . This calculation for different
 915 values of y^+ and for the four Re_τ gives the parametric function presented in figure 16a.

916

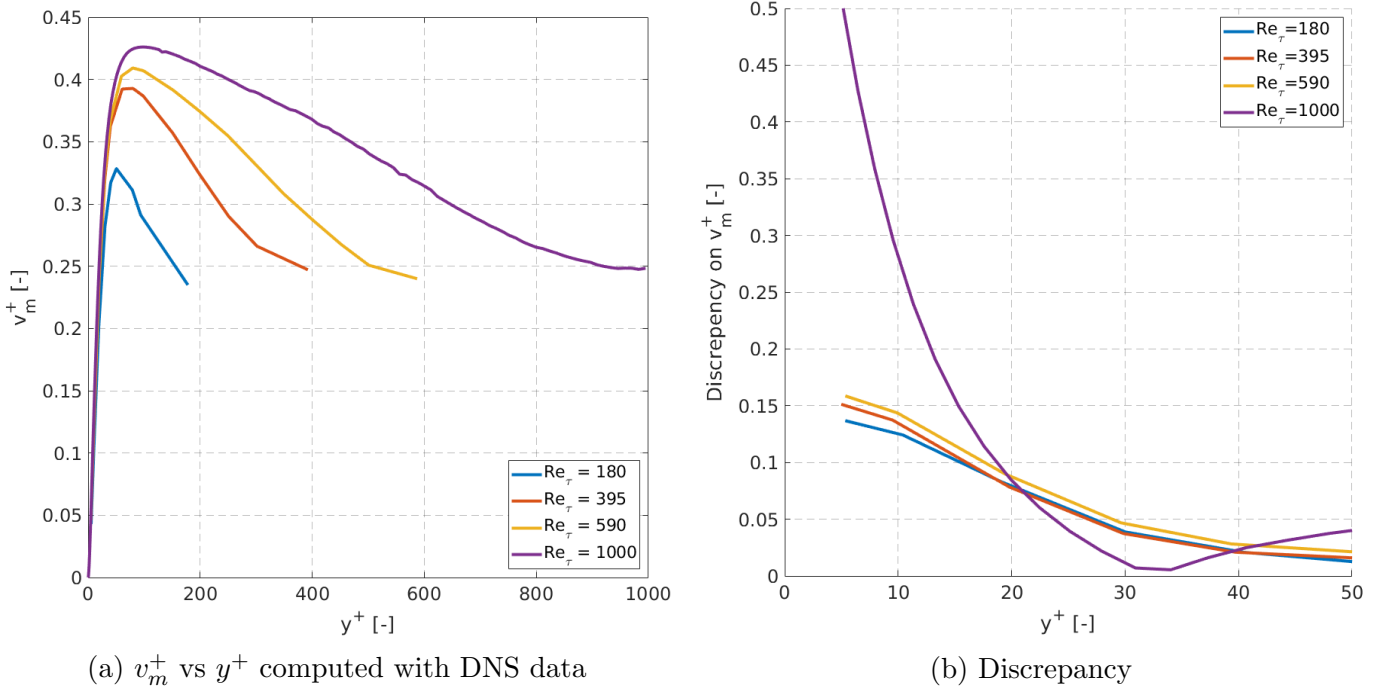


Figure 16: (a) Dimensionless velocity v_m^+ as a function of the dimensionless normal coordinate y^+ calculated for $Re_\tau = 180, 395, 590, 1000$ with DNS data of Moser et al. [33] and Graham et al. [32]. (b) Discrepancies with the Gaussian distribution assumption.

917 **B Appendix - Uncertainty**

918 The uncertainty of δ is defined in the present work as

$$\Delta\delta = \sqrt{(\Delta\delta_m)^2 + (\Delta\delta_t)^2 + (\sigma_\delta)^2} \quad (32)$$

919 $\Delta\delta_m$ is the uncertainty resulted from the propagated measurement uncertainty on the heat flux to
920 water. As reported in Kossolapov et al. [9], the measurement uncertainty of the heat flux to water
921 $\delta q_w''$ is mainly due to the uncertainty of the current and voltage measurements. The latter generates
922 an uncertainty in the computed value of the mantle thickness. To compute this uncertainty $\Delta\delta_m$, the
923 algorithm described in Figure 7 is computed using as input the heat flux $(q_w'' \pm \delta q_w'')(t)$. The difference
924 between the output and the previously computed δ defines then the measurement uncertainty $\Delta\delta_m$.

925

926 $\Delta\delta_t$ is the temporal uncertainty due to the boiling crisis frame assessment [9]. The latter is due
927 to the frame rate of the IR camera which implies that the occurrence of the boiling crisis can only
928 be assessed within a small, but non-null, time interval. To compute this uncertainty $\Delta\delta_t$, the al-
929 gorithm described in Figure 7 is computed using as integration interval the interval $[0, t_{CHF} \pm \delta t]$,
930 with $\delta t = 0.4$ ms, the inverse of the camera frame rate. The difference between the output and the
931 previously computed δ defines then the temporal uncertainty $\Delta\delta_t$.

932

933 Finally, as each working point was tested three times, σ_δ is the standard deviation of the three
934 corresponding values of the mantle thickness, quantifying the repeatably of the process.